

Ultra-high-density double-atom catalyst with spin moment as activity descriptor for oxygen reduction reaction

Peng Lv¹, Wenjing Lv¹, Donghai Wu¹, Gang Tang², Xunwang Yan³, Zhansheng Lu^{4*},
Dongwei Ma^{1*}

¹*Key Laboratory for Special Functional Materials of Ministry of Education, and School of Materials Science and Engineering, Henan University, Kaifeng 475004, China*

²*Advanced Research Institute of Multidisciplinary Science, Beijing Institute of Technology, Beijing 100081, China*

³*College of Physics and Engineering, Qufu Normal University, Qufu 273165, China*

⁴*School of Physics, Henan Normal University, Xinxiang 453007, China*

ABSTRACT

One of the great challenges facing atomically dispersed catalysts, including single-atom catalyst (SAC) and double-atom catalyst (DAC) is their ultra-low metal loading (typically less than 5 wt%), basically limiting the practical catalytic application, such as oxygen reduction reaction (ORR) crucial to hydrogen fuel cell and metal-air battery. Although some important progresses have been achieved on ultra-high-density (UHD) SACs, the reports on UHD-DACs with stable uniform dispersion is still lacking. Herein, based on the experimentally synthesized M_2N_6 motif ($M = \text{Sc-Zn}$), we theoretically demonstrated the existence of the UHD-DACs with the metal loading > 40 wt%, which were confirmed by systematic analysis of dynamic, thermal, mechanical, thermodynamic, and electrochemical stabilities. Furthermore, ORR activities of the UHD-DACs are comparable with or even better than those of the experimentally synthesized low-density (LD) counterparts, and the Fe_2N_6 and Co_2N_6 UHD-DACs locate at the peak of the activity volcano with ultra-low overpotentials of 0.31 and 0.33 V, respectively. Finally, spin magnetic moment of active center is found to be a catalytic descriptor for ORR on the DACs. Our work will stimulate the experimental exploration of the ultra-high-density DACs and provides the novel insight into the relationship between ORR activity of the DACs and their spin states.

* Corresponding author. E-mail: madw@henu.edu.cn, dwmachina@126.com (DW. Ma); zslu@htu.edu.cn (ZS. Lu)

I. INTRODUCTION

The four-electron oxygen reduction reaction (ORR) is a key electrochemical reaction for the renewable energy conversion and storage technologies, due to its significance for metal-air batteries and proton exchange membrane fuel cells (PEMFCs). [1–3] Up to now, Pt-based catalysts are the best-known ORR electrocatalysts for commercial applications. [4–6] However, the large-scale commercialization of Pt-based catalysts is significantly restricted by the low natural reserves, high cost, and limited stability of Pt. Therefore, designing and searching alternative ORR electrocatalysts of low cost, high activity, and long durability is increasingly attractive but with great challenges ahead. [7,8] For example, single-atom catalyst (SAC) with uniform dispersion of transition-metal (TM) active sites coordinated with nitrogen atoms in carbon (termed as M-N-C, such as FeN₄ SAC [9,10]) have gained wide attentions in the past few years. [11–14]

Very recently, double-atom catalyst (DAC) has emerged as a new frontier in heterogenous electrocatalysis due to its synergetic dual atomic sites, which can endow DAC with many intrinsic advantages compared with SAC for the multiple-step coupled electron-proton transfer reactions in electrocatalysis. [15–17] To be specific, for ORR, the dual atomic sites can facilitate the dissociation of the O-O bond of the intermediates tending to adopt the side-on adsorption configuration, which favors the desirable four-electron ORR and hinders the two-electron ORR, thereby promoting the energy efficiency of the ORR process in PEMFCs or metal-air batteries and enhancing the stability of catalysts. [18–23,23–30] Among the various DACs for ORR, the one with each TM metal coordinated with four N atoms in carbon sheet (termed as M₂N₆ DAC as shown in **Fig. S1(a)** within the Supplemental Material [31]) has gained particular attentions, [18,23–29,32,33] for which the basic structural motif, M₂N₆, is shown in **Fig. 1(a)**. Combining experimental and theoretical simulations, the FeMnN₆, FeCoN₆, FeNiN₆, and FeZnN₆ DACs for ORR have been thoroughly investigated, and these systems outperform the corresponding SAC counterparts and even the Pt/C catalysts. [23–26,28,29] For example, electronic synergies between Fe and Mn in FeMnN₆ deliver the better durability and more excellent ORR performance (half-wave potentials are 0.928 and 0.804 V in alkaline condition and acidic media, respectively) than both FeN₄, MnN₄ SACs, and commercial Pt/C catalyst. [24] In addition, besides ORR, M₂N₆ DACs have been also theoretically and experimentally demonstrated to be efficient for the electrocatalytic CO₂ reduction and other reactions. [34–39]

On the other hand, one of the most significant challenges facing the atomically dispersed catalysts is their ultra-low active site density (typically less than 5 wt%), [23–25,27,34,39–43] which leads to their overall poor catalytic performance and limits the future industrialization. For example, for MnFeN₆ DAC mentioned above, the content of Fe and Mn are only 2.3 wt% and 1.6 wt%, respectively. [24] Excitingly, very recently, there already are some breakthroughs

in synthesizing ultra-high-density (UHD) SACs. [44–48] A multilayer stabilization strategy was used to construct SACs with metal loading to 16 wt%. [49] A versatile approach combining impregnation and two-step annealing can successfully synthesize 15 metals on chemically distinct supports with metal contents up to 23 wt%. [50] The metal loading of SAC can even reach up to about 40 wt% by means of a graphene quantum dot assisted synthesis strategy. [51] However, with advantages of DAC compared with SAC in mind, to our best knowledge, there are no UHD-DACs reported up to now, which is the focus of the present study.

Herein, starting from the M_2N_6 motif shown in **Fig. 1(a)**, we tried to construct the UHD-DACs (**Fig. 1(a)**) with as few C atoms as possible as glue, which can reach the metal loading > 40 wt% in weight fraction, corresponding to the 14 at% in atomic metal percentage. For the active center, all the 3d TMs (Sc~Zn) with small atomic radius have been considered, inspired by the experimental reports. [24,26,34,35] Among various UHD-DAC candidates, ten ones were screened out, which exhibit excellent dynamic, thermal, mechanical, thermodynamic, and electrochemical stabilities, comparable to the corresponding low-density (LD) systems (see the atomic models in **Fig. S1(b)**). Furthermore, the ORR reaction mechanism has been comparably investigated for the UHD-DACs and their corresponding LD-DACs (**Fig. S1(b)**). Finally, the relationship between the ORR catalytic activity of the considered DACs and their spin magnetic moment was investigated and uncovered.

II. COMPUTATIONAL DETAILS

All spin-polarized computations were carried out by the generalized gradient approximation (GGA) method with Perdew–Burke–Ernzerhof (PBE) functional [52] based on density functional theory (DFT) implemented in the Vienna *ab initio* Simulation Package (VASP), [53,54] in which van der Waals (vdW) correction proposed by Grimme (DFT+D3) was chosen. [55] The plane-wave basis set with a cut-off energy of 500 eV were employed. A vacuum layer of ~16 Å was used to avoid the interactions between periodic images for all calculations. The convergence thresholds of the total energy and the Hellmann–Feynman force are 10^{-7} eV and 0.0005 eV/Å, respectively. For the structural optimization of primitive cell, various magnetic states have been considered and relaxed by the Monkhorst–Pack meshes of $8 \times 8 \times 1$ and the optimized lattice parameters of the lowest-energy structures are presented in **Table S1**, with the corresponding atomic configurations in **Fig. S1(c)**. The phonon dispersions were calculated with the finite displacement method by using the PHONOPY code. [56] The *ab initio* molecular dynamics (AIMD) simulations for the new UHD-DAC supercells ($2 \times 2 \times 1$) were performed based on the NVT ensemble with a time step of 2 fs and total time of 10 ps. The simulated scanning tunneling microscopy (STM) images were obtained using the Tersoff–Hamann theory. [57]

For the binding energy (E_b), dissolution potential (U_{diss} , versus SHE), and formation energy (E_{form}) of UHD-DACs and corresponding LD-DACs, they can be defined as:

$$E_b = E(\text{total}) - E(\text{CN}) - \mu(\text{M}_1) - \mu(\text{M}_2) \quad (1)$$

$$U_{\text{diss}} = U_{\text{diss}}^\circ(\text{metal, bulk}) - E_b/(eN_e * N_M) \quad (2)$$

$$E_{\text{form}} = E(\text{total}) - 6\mu(\text{N}) - 6\mu(\text{C}) - \mu(\text{M}_1) - \mu(\text{M}_2) \quad (3)$$

where $E(\text{total})$ and $E(\text{CN})$ are the total energies of DAC system and CN composite, respectively; $\mu(\text{M}_1)$, $\mu(\text{M}_2)$, $\mu(\text{N})$, and $\mu(\text{C})$ are the chemical potential of the involved species, which is taken from the metal bulk, N_2 molecules, and graphene, respectively; $U_{\text{diss}}^\circ(\text{metal, bulk})$ and N_e are the standard dissolution potential (pH = 0) of bulk metal in aqueous solution and the number of electrons involved in the dissolution, respectively, which are taken from the previous work [58,59] and has been listed in **Table S4**. N_M indicates the number of metal atoms. The N_M takes 2 for the current DAC system. [60]

The in-plane Young's modulus (E_x , E_y), Poisson's ratio (ν_{xy} , ν_{yx}), and shear modulus (G) along the armchair (x) and zigzag (y) directions for UHD-DACs can be calculated by the following equations: [61]

$$E_x = (C_{11}C_{22} - C_{12}C_{21})/C_{22} \quad (4)$$

$$E_y = (C_{11}C_{22} - C_{12}C_{21})/C_{11} \quad (5)$$

$$\nu_{xy} = C_{21}/C_{22} \quad (6)$$

$$\nu_{yx} = C_{12}/C_{11} \quad (7)$$

$$G = C_{66} \quad (8)$$

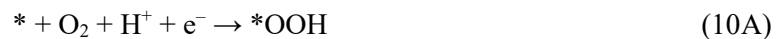
For the ORR related calculations, the standard conventional cells of various UHD-DACs were used as the electrocatalysts and the Monkhorst–Pack meshes of $5 \times 4 \times 1$ and $12 \times 10 \times 1$ are adopted for structural optimization and calculation of densities of states (DOS), respectively. The convergence thresholds of the total energy and the Hellmann–Feynman force are 10^{-5} eV and 0.03 eV/Å, respectively.

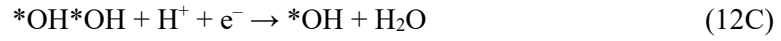
The free energy change (ΔG) under the acidic medium (pH = 0) for each elementary reaction step was calculated based on the computational hydrogen electrode (CHE) model, [62–64] according to the following equation:

$$\Delta G = \Delta E + \Delta E_{\text{ZPE}} - T\Delta S \quad (9)$$

where ΔE is the reaction energy from DFT calculations. ΔE_{ZPE} and $T\Delta S$ ($T = 298.15$ K) are the contributions of the zero-point energy and entropy to ΔG , respectively. E_{ZPE} and TS for the free molecules are taken from the NIST database, [65] and those of the adsorbed species were obtained based on the calculated vibrational frequencies and then with the VASPKIT code. [66] The reaction step with ΔG_{max} is the potential-determining step (PDS).

The ORR has been investigated under the acidic medium (pH = 0), the corresponding elementary reaction steps along the pathway-A, pathway-B, and pathway-C for ORR in **Fig. 3a** can be described as:





The Gibbs adsorption free energy of the intermediates (*OH, *OOH (*O*OH), *OH*OH, and *O) can be evaluated by the following equations:

$$\Delta G (*OH) = G (*OH) + 1/2G (H_2) - G^* - G (H_2O) \quad (14)$$

$$\Delta G (*OOH) = G (*OOH) + 3/2G (H_2) - G^* - 2G (H_2O) \quad (15)$$

$$\Delta G (*O*OH) = G (*O*OH) + 3/2G (H_2) - G^* - 2G (H_2O) \quad (16)$$

$$\Delta G (*OH*OH) = G (*OH*OH) + G (H_2) - G^* - 2G (H_2O) \quad (17)$$

$$\Delta G (*O) = G (*O) + G (H_2) - G^* - G (H_2O) \quad (18)$$

According to the above ΔG values, and setting $\Delta G (O_2) = 4.92$ eV and $\Delta G (H_2O) = 0$ eV, respectively, we can obtain the free energy changes (ΔG_x , for step $x = 1-4$) and equilibrium potential (U_x , $x = 1-4$) as follows:

$$\Delta G_1 = -eU_1 = \Delta G (*OOH) - 4.92 \quad (19A)$$

$$\Delta G_1 = -eU_1 = \Delta G (*O*OH) - 4.92 \quad (19B; 19C)$$

$$\Delta G_2 = -eU_2 = \Delta G (*O) - \Delta G (*OOH) \quad (20A)$$

$$\Delta G_2 = -eU_2 = \Delta G (*O) - \Delta G (*O*OH) \quad (20B)$$

$$\Delta G_2 = -eU_2 = \Delta G (*OH*OH) - \Delta G (*O*OH) \quad (20C)$$

$$\Delta G_3 = -eU_3 = \Delta G (*OH) - \Delta G (*O) \quad (21A; 21B)$$

$$\Delta G_3 = -eU_3 = \Delta G (*OH) - \Delta G (*OH*OH) \quad (21C)$$

$$\Delta G_4 = -eU_4 = -\Delta G (*OH) \quad (22A; 22B; 22C)$$

where A, B and C indicate the pathway-A, pathway-B, and pathway-C for ORR in **Fig. 3a**, respectively. Then the overpotential (η_{ORR} , V) is defined in the following:

$$\eta_{ORR} = (\Delta G_{max}/e) + 1.23 \quad (23)$$

The standard GGA simulations usually underestimates the solvation effect to affect the free energies for ORR under the practical conditions. The continuum solvation model [67] were used to investigate the solvation effect on the ORR. The solvation energies for different adsorbed species are shown in the **Table S6**. These values from continuum solvation model are all negative, indicating that the solvent can stabilize the adsorbates in solution. Also, it is noted that our calculation values are comparable to the previous works. [18,59,68] We also studied the solvation effect for ORR from the explicit water by combining force-field molecular dynamic simulation implemented in LAMMPS, [69,70] *ab initio* molecular dynamics

simulation in VASPsol, [67] and static structural optimization. It is found that the solvation energies from the continuum solvation model by VASPsol are comparable with those from our explicit model and those of previous work. [18,68,71] Moreover, the explicit solvation effect doesn't alter their optimal reaction pathway for ORR on both UHD- and LD-DACs [see Note S1 with corresponding figures and tables in Supplemental Material [31]].

III. RESULTS AND DISCUSSION

A. Morphologies of UHD-DACs

Stimulated by the experimental LD-DAC (**Fig. S1(a)**), we have designed a new kind of 2D material (*i.e.*, the UHD-DAC herein in **Fig. 1(a)**) by extremely reducing the surrounding carbon atoms of dual metal active center. From **Fig. 1(a)**, the lattice structure of M_2N_6 UHD-DACs was constructed by gluing the M_2N_6 motif by six C atom locating at the corner of primitive cell, which realize a minimum cell containing a pair of TM atoms (TM = Sc~Zn). Thus, the geometric structure of active center for the designed UHD-DACs is the same as that of experimentally prepared LD-DAC, but the former achieves a unprecedentedly ultra-high density of active center with metal loading up to 36 to 46 wt% for DACs in weight fraction, which catch up with the recently reported ultra-high-density Ir-N-C SAC (~40 wt%). [51] From the view of atomic metal percentage, [72] here the UHD-DACs present the high metal contents of 14.3 at%, about 4 times larger than that of the Ir-N-C SAC (3.8 at%). [51] For the structural optimization, the optimized lattice parameters of the lowest-energy structures are presented in **Table S1**, with the corresponding atomic configurations in **Fig. S1(c)**. For all the cases, the systems have the 2D rhombus lattice of primitive cell, while they own the 2D rectangular conventional cell, dissimilar to the well-known lattice symmetry of graphene. The homonuclear (heteronuclear) UHD-DAC structures possess the space group of $Cmmm$ ($Amm2$) with the point group D_{2h} (C_{2v}) symmetry, which both belong to the orthorhombic phase. As a contrast, the theoretical model of experimentally synthesized LD-DACs was also built by embedding the same M_2N_6 active center in 3×6 rectangular supercells (**Fig. S1(b)**) for simulations.

B. Dynamic, thermal, mechanical, thermodynamic, and electrochemical stabilities of UHD-DACs

We comprehensively examined their stabilities from five aspects: dynamic, thermal, mechanical, thermodynamic, and electrochemical stabilities (**Fig. 1(b)**). The constructed UHD-DAC would be considered stable if it meets all the stability criteria (**Fig. S2**). First, the dynamic stability of the homonuclear M_2N_6 UHD-DACs was verified by calculating their phonon dispersions, which describes the dispersion relations of lattice vibrations and usually identifies as the decisive factor for materials' stability. From **Fig. 2(a)** and **Fig. S3**, we can find that only homonuclear Mn_2N_6 , Fe_2N_6 , Co_2N_6 , and Ni_2N_6 UHD-DACs are dynamically stable as indicated by the absence of the obvious imaginary phonon frequencies. Small atomic radii of Mn, Fe, Co, and Ni correspond to the relatively small lattice constants and compact lattice interactions [73]

of UHD-DACs, which are response for the dynamic stability of homonuclear Mn_2N_6 , Fe_2N_6 , Co_2N_6 , and Ni_2N_6 UHD-DACs. Based on this result, it is expected that the heteronuclear UHD-DACs formed by the pairwise combination of these four elements also have the good dynamic stability. Thus, we also investigated the phonon dispersions of six heteronuclear M_2N_6 UHD-DACs, *i.e.*, MnFeN_6 , MnCoN_6 , MnNiN_6 , FeCoN_6 , FeNiN_6 , and CoNiN_6 (**Fig. S3**). Like their corresponding homonuclear ones, they also possess the great dynamic stability without any imaginary frequencies. It is noticed that all the UHD-DAC structures have 52 phonon vibrational modes, which are 3 acoustic modes and 49 optical modes. Through group theory analysis, the irreducible representation of the optical branches at the Brillouin-zone with Raman (R) and infrared (IR) symbols for the homonuclear and heteronuclear UHD-DAC structures are as follows: $\Gamma_{\text{optic}}(\text{homonuclear}) = 7A_g(\text{R}) + 2A_u + 7B_{1g}(\text{R}) + 4B_{1u}(\text{IR}) + 3B_{2g}(\text{R}) + 6B_{2u}(\text{IR}) + 4B_{3g}(\text{R}) + 6B_{3u}(\text{IR})$; $\Gamma_{\text{optic}}(\text{heteronuclear}) = 13A_1(\text{R/IR}) + 6A_2(\text{R}) + 7B_1(\text{R/IR}) + 13B_2(\text{R/IR})$. We hope here the Raman and IR Brillouin spectroscopy measurements in the further experiments will test and verify the accuracy of the calculations in our theoretical modeling.

Furthermore, *ab initio* Molecular Dynamics (AIMD) simulations were performed to check the thermal stability under ambient conditions of these 10 M_2N_6 UHD-DACs with dynamic stability. Note that their total free energy only shows the periodic oscillating near the equilibrium state during the entire simulation period of 10 ps at 500 K (**Fig. 2(b)** and **Fig. S4**). Simulation snapshots of the M_2N_6 UHD-DACs also show their structural integrity at 10 ps, implying their thermal stability. In addition, we calculated their elastic constants (**Table S3**) of M_2N_6 UHD-DACs using the finite differences method [74] with assuming a thickness of 3.34 Å on the basis of graphene's thickness [75] to check their mechanical stability. Significantly, these values satisfy the requirements of the mechanical stability criterion [76,77] of a 2D material, *i.e.*, $C_{11} \times C_{22} - C_{12}^2 > 0$ and $C_{66} > 0$. The in-plane Young's modulus (Y , GPa), Poisson's ratio (ν), and shear modulus (G , GPa) were obtained from the elastic constants, which are summarized in **Table S3**. Also, the 2D directional projection in polar coordinates of the Young's modulus, Poisson's ratio, and shear modulus of Fe_2N_6 UHD-DAC are displayed in **Fig. 2(c)**, and those for other systems are illustrated in **Fig. S5**. The mechanical results in **Fig. 2(c)**, **Fig. S5**, and **Table S3** show that the in-plane Young's modulus and Poisson's ratio along the armchair direction are larger than that along the zigzag direction, revealing the moderate anisotropy of the mechanical properties. Also, it is noted that the Young's modulus of all the UHD-DACs are much smaller than that of graphene (~ 1000 GPa), [75,78] indicating that these UHD-DACs are softer than the well-known graphene and suitable for the strain-tunable catalysis. [79]

The thermodynamic stability of ten UHD-DACs was examined by the binding energy (E_b), as shown in **Fig. 2(d)** and **Table S4**. The more negative E_b values indicates the stronger chemical bond formed between the metal atoms and the coordinated N atoms. We can see that,

the E_b values for all the ten UHD-DACs are more negative than -5 eV, which can effectively prevent the diffusion and aggregation of the metal atoms, promising high thermodynamic stability of the whole systems. For comparison, the E_b for the corresponding LD-DACs were also calculated, and the E_b values of UHD-DACs are only slightly positive than those of the corresponding LD-DACs, suggesting that the high density of metal loading will not affect the thermodynamic stability of current DAC systems.

The electrochemical stability of electrocatalyst is one of the key factors for its practical application in an electrochemical environment. [59] According to its definition in the Computational Details, the more positive dissolution potential (U_{diss}) suggests that the metal dimer strongly bind with the coordinated atoms in the UHD-DAC system and the dissolution of metal atoms can be avoided under the acidic conditions (pH = 0). To this end, we calculated the U_{diss} of above ten UHD-DAC systems, as illustrated in **Fig. 2(e)** and **Table S4**. Here we use the range of $U_{\text{diss}} > 0$ V to measure the electrochemical stability, which is a valid evaluation criterion that has been widely used in the literatures. [59,80] Given that all ten DAC systems have the positive U_{diss} values, the metal dimers in the corresponding UHD-DACs (Mn_2N_6 , Fe_2N_6 , Co_2N_6 , Ni_2N_6 , MnFeN_6 , MnCoN_6 , MnNiN_6 , FeCoN_6 , FeNiN_6 , and CoNiN_6) with the dynamic, thermal, mechanical, and thermodynamic stability can survive under the experimentally electrochemical conditions, suggesting their excellent electrochemical stability.

C. Synthesis feasibility and electronic properties of UHD-DACs

Then the feasibility of experimental realization of these ten UHD-DACs is explored by calculating the formation energies (E_{form}) following in Computational Details. As shown in **Fig. 2(f)** and **Table S4**, their E_{form} values range from about 1.7 to 3.1 eV and are generally smaller than those of another kinds of M_2N_6 catalysts with double MN_3 groups. [81,82] We also observed that the formation energies of Ni_2N_6 , FeNiN_6 , and CoNiN_6 UHD-DACs are lower than or comparable with those of the corresponding synthesized ones with low metal contents. [23,28,29,39,43] Noted that the values of E_{form} values depend on the chemical potentials of the involved species, which in turn depends on the experimental conditions. Therefore, it is the relative values of E_{form} that determine the formation probability of a specific system among various ones and it is also expected that all the proposed UHD-DAC systems with dynamic, thermal, mechanical, thermodynamic, and electrochemical stabilities are suitably synthesizable in the experiments. Moreover, the calculated E_{form} values of UHD-DACs also indicate the thermodynamical stability of N-N motif and suppression of N_2 gas formation in the UHD-DACs because all these values are lower than that the experimentally synthesized Ni_2N_6 LD-DAC (3.22 eV). [39] Hence, we also theoretically predicted the STM images of these ten stable UHD-DACs with 8×8 supercells for the future experimental identification, as shown in **Fig. 2(g)** and **Fig. S6**. It is easy to recognize and correlate them with the corresponding atomic structure of metal dimers, while the C and N atoms are difficult to identify because they

are lighter and then brighter than the metal ones.

We further investigated the electronic properties of these ten stable UHD-DACs, including the electron localization function (ELF) and density of states (DOS). The bonding characters can be effectively characterized by ELF. As shown in **Fig. S7**, the electrons are more localized around C and N atoms with larger ELF values, while more delocalized around metal atoms with smaller ELF values, indicating the strong covalent bonding characteristics for C-C, C-N, N-N, and Fe-N interactions and metallic bonding features of metal dimers, which is responsible for the good stability of the UHD-DACs. Importantly, the calculated total DOS (TDOS) and partial DOS (PDOS) based on PBE and HSE06 functional [83] presented in **Fig. S8-9**, suggest the metallic conductivity feature of all stable UHD-DACs, beneficial for the charge transfer during the electrocatalytic ORR process. Finally, for most of the systems there are large spin magnetic moments localized on the anchored metal atoms, which benefit the effective adsorption and activation of the oxygenated intermediates. [84–86] However, the spin magnetic moments of the embedded Ni atoms are fully quenched in the Ni₂N₆ and CoNiN₆ UHD-DACs, probably due to the charge transfer and the electronic state coupling.

D. Scaling relationship for adsorption of key intermediates

Following the comprehensive assessment of the overall stabilities and electronic properties of ten UHD-DACs, we investigated their ORR catalytic activity, as well as that of the corresponding LD-DACs. Considering the dual metal sites of DACs, three reaction pathways for ORR have been considered under acidic conditions (pH = 0). The traditional ORR pathway over the catalysts is shown in **Fig. 3(a)**: the protonation of *OOH to produce the first H₂O molecule and the continuous hydrogenation of the remaining *O atom to yield the second H₂O molecule (pathway-A). Moreover, the dual-metal sites may facilitate the breaking of the O-O bond of *OOH as described in **Fig. 3(a)** to drive the ORR following the pathway-B or pathway-C. [19,87] All the three pathways have been considered for ORR to obtain the most energetically feasible ones.

In fact, there are two mechanisms for the first electron transfer process of ORR. [88] One is that the process of short-range electron transfer to adsorbed O₂ occurs in the inner Helmholtz plane (ET-IHP mechanism), for which O₂ protonates in the catalyst surface to form the *OOH. Another is that the process of long-range electron transfer to non-adsorbed O₂ occurs in the outer Helmholtz plane (ET-OHP mechanism), for which O₂ protonates in the electrolytes and subsequently adsorbs at active site as *OOH. However, the ET-IHP mechanism usually occurs on Pt based noble metal catalyst. For the SACs and DACs, the ET-OHP mechanism is usually considered to be the relevant one. [11,26] Thus, we focused on the latter ET-OHP mechanism that does not rely on direct adsorption of O₂ to the catalyst surface and the initial stage for ORR is the gas phase O₂.

Firstly, we investigated the adsorption of key intermediates, including *O, *OOH, *O*OH,

*OH*OH, and *OH, and the scaling relationship between their binding strengths (*O and *OOH versus *OH (pathway-A); *O and *O*OH versus *OH (pathway-B); *OH*OH and *O*OH versus *OH (pathway-C)). From **Fig. 3(b)-(d)**, we can see that for UHD-DACs pathway-A exhibits an excellent linear scaling relationship between the binding strengths of the oxygenated intermediates with $R^2 = 0.99$ and 0.98 for ΔG (*O) and ΔG (*OOH) versus ΔG (*OH), respectively. For pathway-B, the binding strength of *O and *OH is also well correlated with $R^2 = 0.98$. However, the binding strengths between *O*OH or *OH*OH and *OH for pathway-B and C display relatively poor linear relationship (with $R^2 < 0.71$), which could help to achieve better ORR activity due to the deviation of the linear scaling relationship. Moreover, this poor scaling relation can be ascribed to the different adsorption modes of *O*OH and *OH*OH, both of which bind with the active sites through two metal atoms, compared with *OH binding through one metal atom (**Fig. S10**). The flexible dual-atom active sites induced decoupling binding strength between the key intermediates have been observed in other reactions, such as electrocatalytic CO₂ reduction and N₂ reduction. [89–91] Note that for the LD-DAC systems, comparatively, the scaling relationship between the binding strengths of key intermediates (**Fig. S11**) have the similar linear trends with the above UHD-DACs.

E. ORR catalytic activity of UHD-DACs

For the three ORR pathways, the reaction free energy diagrams on UHD-DACs under different potentials are shown in **Fig. S12-S14**, and the theoretical overpotentials (η_{ORR}) for the most favorable pathway are summarized in **Fig. 3(e)**. We can observe that the homonuclear Mn₂N₆, Fe₂N₆, and Co₂N₆ UHD-DACs prefers to the pathway-C, in which the O-O bond of *OOH is broken and *OH*OH species is formed with each O atom binding with one metal atom. The heteronuclear UHD-DACs (except CoNiN₆ with pathway-A) tend to adopt the pathway-B, where the dissociated *OOH, i.e., *O*OH, is reduced to *O. Among them, Fe₂N₆ and Co₂N₆ UHD-DACs have the smallest η_{ORR} of 0.31 and 0.33 V along the optimal pathway-C, respectively, delivering the highest ORR activity among all the UHD-DACs. Note that the η_{ORR} of Fe₂N₆ and Co₂N₆ UHD-DACs are smaller than that for the state-art commercial Pt/C catalyst (0.45 V). [1,92] Moreover, interestingly, the Fe- and Co-based heteronuclear UHD-DACs also have the relatively good catalytic activity, in which the MnFeN₆, MnCoN₆, FeCoN₆, FeNiN₆, and CoNiN₆ UHD-DACs possess the η_{ORR} of 0.66, 0.68, 0.51, 0.52, and 0.59 V, respectively. For comparison, we also investigated the ORR activity over the corresponding LD-DACs, for which the free energy diagrams are presented in **Fig. S15-17**, and the η_{ORR} of the optimal pathways are also summarized in **Fig. 3(e)**. We can see the η_{ORR} for all the UHD-DACs (except Co₂N₆) are comparable with those of the corresponding LD-DACs, indicating that the UHD-DACs can well maintain the intrinsic ORR activity of the active centers. Interestingly, the Co₂N₆ UHD-DAC even exhibits much higher ORR activity than its LD-DAC

case. More significantly, FeMnN₆, FeCoN₆, FeNiN₆, and FeZnN₆ DACs have been definitely determined to exhibit excellent catalytic performances for the ORR. [23–26,28,29] Overall, the excellent stabilities and ORR catalytic activities render the proposed UHD-DACs promising ORR electrocatalysts with ultra-high-density active sites available.

Moreover, we considered the competitive reactions on the UHD-DACs, including the two-electron ORR and hydrogen evolution reaction (HER). The results show that most of the concerned UHD-DACs have the good selectivity for four-electron ORR toward H₂O (see the details in Supplemental Material [31] with **Table S5**).

To better understand the ORR catalytic trend, the η_{ORR} as a function of ΔG (*OH) are plotted in **Fig. 4**. It can be found that for the pathway-A (**Fig. 4(a)**), pathway-B (**Fig. 4(b)**), and pathway-C (**Fig. 4(c)**), when ΔG (*OH) reaches about 0.9, 1.0, and 1.0 eV, respectively, the DAC systems possess the highest ORR catalytic activity (the lowest η_{ORR}), and the weaker or stronger binding of *OH on the active sites will lead to the deteriorated ORR activity. Consequently, a volcanic relationship between η_{ORR} and ΔG (*OH) can be observed for all the reaction pathways. Thus, ΔG (*OH) can serve as an effective ORR activity descriptor for the studied DAC systems. Moreover, for the optimal reaction pathways of each DAC (**Fig. 4(d)**), the appropriate binding strength of *OH on Fe₂N₆ and Co₂N₆ UHD-DACs prompts the equilibrium between oxygenated species activation and catalyst recovery and then results in the highest activity among all the UHD-DACs.

F. Spin as universal descriptor for both UHD- and LD-DACs

Recent studies show that the spin magnetic moment of the active center is a novel activity descriptor for the ORR on SACs, which is an intrinsic physical property. [93] For example, the larger spin magnetic moments can induce a better catalytic activity for ORR on the FeN₄ based SACs because the spin electrons are beneficial for binding and activation of reaction intermediates. [94] Correspondingly, we investigated the possibility of the spin magnetic moment as ORR activity descriptor herein. Interestingly, as shown in **Fig. 5(a)**, ΔG (*OH) for all UHD- and LD-DAC systems are correlated linearly with spin magnetic moments M_S of the metal atom that binds OH ($R^2 = 0.87$), which shows that the larger spin magnetic moment contributes to the stronger adsorption of *OH. This strong linear correlation suggests that M_S can function as an efficient descriptor to predict the ORR catalytic activity. As expected, as shown in **Fig. 5(b)**, the η_{ORR} indeed exhibits a volcano relationship with M_S , and importantly M_S is a unified descriptor for both UHD- and LD-DAC systems.

Importantly, the excellent linear relationship between ΔG (*OH) and M_S , and volcano relationship between ΔG (*OH) and η_{ORR} , have also been confirmed by the HSE06 functional (**Fig. S19**). From **Fig. S19(a)** and **Fig. S19(c)**, there is a good linear scaling relationship between M_S and ΔG (*OH) both for PBE and HSE methods, with the linear slope of -0.47 and -0.35,

respectively. The relatively smaller M_S for magnetic active center by PBE method is responsible for the more negative slope, compared with that from HSE method. Moreover, there is a good volcanic relationship for η_{ORR} as a function of M_S for PBE and HSE calculations (**Fig. S19(b)** and **Fig. S19(d)**). It is found that the critical M_S corresponding to the theoretical optimal activity by PBE ($0.94 \mu_B$) is smaller than that based on HSE functional ($1.32 \mu_B$), which also stems from the smaller M_S for magnetic active center by PBE method. These results suggest that the spin related conclusions are reliable from PBE method, and as one of the key points in our work, spin magnetic moment of active center by PBE functional indeed can act as a catalytic descriptor for ORR on the DACs, similar to that by HSE functional.

Finally, we explored the mechanism for the significantly enhanced ORR activity of Co_2N_6 UHD-DAC compared with its LD-DAC counterpart, for which the free energy diagrams are presented in **Figs. 6(a)** and **6(b)**. From above, we know that excellent ORR activity of Co_2N_6 UHD-DAC results from its proper binding of $^*\text{OH}$, which correlates with the spin magnetic moment of the active center. Therefore, we comparatively studied the spin magnetic states of Co_2N_6 UHD-DAC and LD-DAC. As presented in **Figs. 6(c)** and **6(d)**, the PDOS show that the Co $3d$ orbitals are asymmetric in UHD-DAC system while symmetric in LD-DAC system, indicating the (non)magnetic states of Co atoms for (LD-) UHD-DAC. Moreover, the Co d_{x^2} , d_{xz} , and d_{yz} in-plane orbitals mainly contribute to the spin magnetic moment of the Co atom in UHD-DAC.

Based on the crystal field theory, the Co cation in the CoN_4 square planar crystal field for SAC system possesses the $3d^7$ electronic configuration, [95] which should have the unpaired electrons and give rise to the spin magnetic state. However, in the current DAC systems, there are double CoN_4 square planar crystal field interacting each other. For the Co_2N_6 LD-DAC, the short Co-Co distance (2.25 \AA) can intensively share the d orbital electrons, resulting in the faultlessly pairing of in-plane d orbital electrons (d_{x^2} , d_{xz} , and d_{yz}) and the completely quenching of spin magnetic moment in LD-DAC. In contrast, a large Co-Co distance (2.45 \AA) in UHD-DAC contributes to the retention of the spin magnetic moment. The spin density distribution in the illustrations of **Figs. 6(c)** and **6(d)** can also confirm our above analysis about the difference of spin magnetic states between Co_2N_6 UHD- and LD-DACs.

In addition, we studied the electronic state interaction between Co $3d$ and $^*\text{OH } 2sp$, for which the PDOS are presented in **Fig. S20**, and furthermore a quantitative analysis in **Figs. 6(e)** and **6(f)**, resorting to the crystal orbital Hamilton populations (COHP). For Co_2N_6 UHD-DAC, the adsorption of $^*\text{OH}$ almost leads to the complete spin quenching of the Co atom that binds it (see **Fig. S20**), and thus the spin-up and spin-down bands contribute similar binding strengths with the integrated COHP (ICOHP) of -1.23 and -1.16 eV , respectively. On the contrary, for Co_2N_6 LD-DAC, the adsorption of $^*\text{OH}$ can induce spin magnetic moment on the Co atoms. Significantly, spin-up bands contribute the similar binding strength, compared with the case of

Co₂N₆ UHD-DAC, with ICOHP of -1.20 eV, while much more occupation of the antibonding state for spin-down bands leads to the much smaller contribution to *OH binding with ICOHP of -0.85 eV. Consequently, Co₂N₆ UHD-DAC binds *OH much stronger than Co₂N₆ UHD-DAC, and exhibits high ORR activity.

IV. CONCLUSIONS

In summary, we theoretically confirmed the existence of ultra-high-density DACs with metal loading > 40 wt%, constructed from the experimentally synthesized M₂N₆ motif. Among the investigated systems, ten ones (Mn₂N₆, Fe₂N₆, Co₂N₆, Ni₂N₆, MnFeN₆, MnCoN₆, MnNiN₆, FeCoN₆, FeNiN₆, and CoNiN₆) were demonstrated to have well dynamic, thermal, mechanical, thermodynamic, and electrochemical stabilities. Mechanism studies on ORR show that most of the UHD-DACs have comparable ORR activities with the corresponding LD-DACs, and Fe₂N₆ and Co₂N₆ UHD-DACs locate at the peak of the activity volcano with the ultra-low overpotentials of 0.31 and 0.33 V, respectively. Furthermore, we investigated the relationship between the ORR activities and the spin states of the active centers, and identified that the spin magnetic moment of active centers of the DACs can serve as an effective catalytic descriptor. Interestingly, Co₂N₆ UHD-DACs exhibit significantly enhanced ORR activity compared with the Co₂N₆ LD counterpart, which can be ascribed to the distortion of the square planar crystal field induced spin state crossover. In addition, the simulated STM images and symmetry classifications of phonon modes for the UHD-DAC systems provide a basis for the future experimental confirmation. We hope our prediction will simulate the experimental exploration of ultra-high-density DACs for practical catalytic applications, and the identified activity descriptor, spin magnetic moment, will guide the rational design of efficient DACs based on spin-state regulation.

ACKNOWLEDGEMENTS

This work is supported by the National Natural Science Foundation of China (Grant No. 12204151, 12274118), the Program for Science & Technology Innovation Talents in Universities of Henan Province (Grant No. 20HASTIT028), the Special Project for Fundamental Research in University of Henan Province (No. 22ZX013), the China Postdoctoral Science Foundation (Grant No. 2022M711048), and the Open Project Program of Guangdong Provincial Key Laboratory of Electronic Functional Materials and Devices, Huizhou University (EFMD2022009M). The work was carried out at National Supercomputer Center in Tianjin, and this research was supported by TianHe Qingsuo Project-special fund project.

REFERENCES

- [1] A. Kulkarni, S. Siahrostami, A. Patel, and J. K. Nørskov, *Understanding Catalytic Activity Trends in the Oxygen Reduction Reaction*, Chem. Rev. **118**, 2302 (2018).
- [2] R. Chattot, O. Le Bacq, V. Beermann, S. Kühl, J. Herranz, S. Henning, L. Kühn, T. Asset, L.

- Guétaz, and G. Renou et al., *Surface Distortion as a Unifying Concept and Descriptor in Oxygen Reduction Reaction Electrocatalysis*, Nat. Mater. **17**, 827 (2018).
- [3] X. Tian, X. F. Lu, B. Y. Xia, and X. W. (David) Lou, *Advanced Electrocatalysts for the Oxygen Reduction Reaction in Energy Conversion Technologies*, Joule **4**, 45 (2020).
- [4] X. Huang, Z. Zhao, L. Cao, Y. Chen, E. Zhu, Z. Lin, M. Li, A. Yan, A. Zettl, and Y. M. Wang et al., *High-Performance Transition Metal-Doped Pt₃Ni Octahedra for Oxygen Reduction Reaction*, Science **348**, 1230 (2015).
- [5] M. Li, Z. Zhao, T. Cheng, A. Fortunelli, C.-Y. Chen, R. Yu, Q. Zhang, L. Gu, B. V. Merinov, and Z. Lin et al., *Ultrafine Jagged Platinum Nanowires Enable Ultrahigh Mass Activity for the Oxygen Reduction Reaction*, Science **354**, 1414 (2016).
- [6] X. Yang, X. Zhang, Z. Lu, Z. Yang, and R. Wu, *Design of Highly Stable and Efficient Bifunctional MXene-Based Electrocatalysts for Oxygen Reduction and Evolution Reactions*, Phys. Rev. Appl. **15**, 044053 (2021).
- [7] U. Martinez, S. Komini Babu, E. F. Holby, H. T. Chung, X. Yin, and P. Zelenay, *Progress in the Development of Fe-Based PGM-Free Electrocatalysts for the Oxygen Reduction Reaction*, Adv. Mater. **31**, 1806545 (2019).
- [8] X. F. Lu, Y. Fang, D. Luan, and X. W. D. Lou, *Metal–Organic Frameworks Derived Functional Materials for Electrochemical Energy Storage and Conversion: A Mini Review*, Nano Lett. **21**, 1555 (2021).
- [9] S. Liu, C. Li, M. J. Zachman, Y. Zeng, H. Yu, B. Li, M. Wang, J. Braaten, J. Liu, and H. M. Meyer et al., *Atomically Dispersed Iron Sites with a Nitrogen–Carbon Coating as Highly Active and Durable Oxygen Reduction Catalysts for Fuel Cells*, Nat. Energy **7**, 652 (2022).
- [10] W. Zhang, Q. Fu, Q. Luo, L. Sheng, and J. Yang, *Understanding Single-Atom Catalysis in View of Theory*, JACS Au **1**, 2130 (2021).
- [11] C. Tang, L. Chen, H. Li, L. Li, Y. Jiao, Y. Zheng, H. Xu, K. Davey, and S.-Z. Qiao, *Tailoring Acidic Oxygen Reduction Selectivity on Single-Atom Catalysts via Modification of First and Second Coordination Spheres*, J. Am. Chem. Soc. **143**, 7819 (2021).
- [12] C. Zhu, Q. Shi, B. Z. Xu, S. Fu, G. Wan, C. Yang, S. Yao, J. Song, H. Zhou, and D. Du et al., *Hierarchically Porous M–N–C (M = Co and Fe) Single-Atom Electrocatalysts with Robust MN_x Active Moieties Enable Enhanced ORR Performance*, Adv. Energy Mater. **8**, 1801956 (2018).
- [13] J. Kim, J. M. Yoo, H. S. Lee, Y.-E. Sung, and T. Hyeon, *Single-Atom M–N–C Catalysts for Oxygen Reduction Electrocatalysis*, Trends Chem. **3**, 779 (2021).
- [14] J. Liu, X. Wan, S. Liu, X. Liu, L. Zheng, R. Yu, and J. Shui, *Hydrogen Passivation of M–N–C (M = Fe, Co) Catalysts for Storage Stability and ORR Activity Improvements*, Adv. Mater. **33**, 2103600 (2021).
- [15] Y. Wang, X. Cui, J. Zhang, J. Qiao, H. Huang, J. Shi, and G. Wang, *Advances of Atomically Dispersed Catalysts from Single-Atom to Clusters in Energy Storage and Conversion Applications*, Prog. Mater. Sci. **128**, 100964 (2022).
- [16] Y. Ying, X. Luo, J. Qiao, and H. Huang, *“More Is Different:” Synergistic Effect and Structural Engineering in Double-Atom Catalysts*, Adv. Funct. Mater. **31**, 2007423 (2021).
- [17] R. Li and D. Wang, *Superiority of Dual-Atom Catalysts in Electrocatalysis: One Step Further Than Single-Atom Catalysts*, Adv. Energy Mater. **12**, 2103564 (2022).
- [18] W. Zou, R. Lu, X. Liu, G. Xiao, X. Liao, Z. Wang, and Y. Zhao, *Theoretical Insights into*

Dual-Atom Catalysts for the Oxygen Reduction Reaction: The Crucial Role of Orbital Polarization, J. Mater. Chem. A **10**, 9150 (2022).

- [19] J. Wang, Z. Huang, W. Liu, C. Chang, H. Tang, Z. Li, W. Chen, C. Jia, T. Yao, and S. Wei et al., *Design of N-Coordinated Dual-Metal Sites: A Stable and Active Pt-Free Catalyst for Acidic Oxygen Reduction Reaction*, J. Am. Chem. Soc. **139**, 17281 (2017).
- [20] Y. He, X. Yang, Y. Li, L. Liu, S. Guo, C. Shu, F. Liu, Y. Liu, Q. Tan, and G. Wu, *Atomically Dispersed Fe–Co Dual Metal Sites as Bifunctional Oxygen Electrocatalysts for Rechargeable and Flexible Zn–Air Batteries*, ACS Catal. **12**, 1216 (2022).
- [21] Q. An, J. Jiang, W. Cheng, H. Su, Y. Jiang, and Q. Liu, *Recent Advances in Dual-Atom Site Catalysts for Efficient Oxygen and Carbon Dioxide Electrocatalysis*, Small Methods **6**, 2200408 (2022).
- [22] J. Zhang, A. Yu, and C. Sun, *Computational Exploration of Dual Atom Catalysts Loaded on Defective Graphene for Oxygen Reduction Reaction*, Appl. Surf. Sci. **605**, 154534 (2022).
- [23] Y. Zhou, W. Yang, W. Utetiwabo, Y. Lian, X. Yin, L. Zhou, P. Yu, R. Chen, and S. Sun, *Revealing of Active Sites and Catalytic Mechanism in N-Coordinated Fe, Ni Dual-Doped Carbon with Superior Acidic Oxygen Reduction than Single-Atom Catalyst*, J. Phys. Chem. Lett. **11**, 1404 (2020).
- [24] G. Yang, J. Zhu, P. Yuan, Y. Hu, G. Qu, B.-A. Lu, X. Xue, H. Yin, W. Cheng, and J. Cheng et al., *Regulating Fe-Spin State by Atomically Dispersed Mn-N in Fe-N-C Catalysts with High Oxygen Reduction Activity*, Nat. Commun. **12**, 1734 (2021).
- [25] H. Li, S. Di, P. Niu, S. Wang, J. Wang, and L. Li, *A Durable Half-Metallic Diatomic Catalyst for Efficient Oxygen Reduction*, Energy Environ. Sci. **15**, 1601 (2022).
- [26] X. Zhou, J. Gao, Y. Hu, Z. Jin, K. Hu, K. M. Reddy, Q. Yuan, X. Lin, and H.-J. Qiu, *Theoretically Revealed and Experimentally Demonstrated Synergistic Electronic Interaction of CoFe Dual-Metal Sites on N-Doped Carbon for Boosting Both Oxygen Reduction and Evolution Reactions*, Nano Lett. **22**, 3392 (2022).
- [27] M. Liu, H. Chun, T.-C. Yang, S. J. Hong, C.-M. Yang, B. Han, and L. Y. S. Lee, *Tuning the Site-to-Site Interaction in Ru–M (M = Co, Fe, Ni) Diatomic Electrocatalysts to Climb up the Volcano Plot of Oxygen Electroreduction*, ACS Nano **16**, 10657 (2022).
- [28] J. Yan, M. Tian, R. Shi, T. Gu, K. Zeng, J. Zhou, Q. Zhang, M. H. Rummeli, and R. Yang, *Enhanced Dual Atomic Fe-Ni Sites in N-Doped Carbon for Bifunctional Oxygen Electrocatalysis*, Mater. Today Energy **101171** (2022).
- [29] H. Li, J. Wang, R. Qi, Y. Hu, J. Zhang, H. Zhao, J. Zhang, and Y. Zhao, *Enhanced Fe 3d Delocalization and Moderate Spin Polarization in FeNi Atomic Pairs for Bifunctional ORR and OER Electrocatalysis*, Appl. Catal. B-Environ **285**, 119778 (2021).
- [30] F. Wang, W. Xie, L. Yang, D. Xie, and S. Lin, *Revealing the Importance of Kinetics in N-Coordinated Dual-Metal Sites Catalyzed Oxygen Reduction Reaction*, J Catal. **396**, 215 (2021).
- [31] See Supplemental Material at [Http://Link.Aps.Org/Supplemental/XXX](http://Link.Aps.Org/Supplemental/XXX) for the Structural Parameters of UHD-DACs; Spin Magnetic Moments of UHD- and LD-DACs; Mechanical Values of UHD-DACs; E_b , U_{diss} , and E_{form} Values for UHD- and LD-DACs; Atomic Model for Experimental M_2N_6 LD-DAC and Our Constructed UHD-DAC; Screening Strategy with Limiting Criterion for the Selection of Stable UHD-DACs; Phonon Dispersions, AIMD Simulation Results, 2D Projections of Mechanical Properties, Simulated STM Images, ELF

- Maps, and DOS of Various UHD-DACs; Atomic Configurations of *OOH, *O*OH, *OH*OH, *O, and *OH Species on Fe₂N₆ and MnFeN₆ UHD-DACs; Scaling Relationship of Adsorption for Key Intermediates; Free Energy Diagrams of ORR for All Stable UHD- and LD-DACs for Pathway-A, B, and C; PDOS with Electronic Orbital Interaction for Co₂N₆ UHD- and LD-DACs with *OH Adsorption; Selectivity Analysis; Solvation Effect Analysis with Solvation Energies for Different Adsorbed Species, which includes Refs. [18, 58-59, 67-71].
- [32] Y. Meng, C. Yin, K. Li, H. Tang, Y. Wang, and Z. Wu, *Improved Oxygen Reduction Activity in Heteronuclear FeCo-Codoped Graphene: A Theoretical Study*, ACS Sustainable Chem. Eng. **7**, 17273 (2019).
 - [33] Y. Sun, J. Wang, Q. Liu, M. Xia, Y. Tang, F. Gao, Y. Hou, J. Tse, and Y. Zhao, *Itinerant Ferromagnetic Half Metallic Cobalt–Iron Couples: Promising Bifunctional Electrocatalysts for ORR and OER*, J. Mater. Chem. A **7**, 27175 (2019).
 - [34] C. Liu, T. Li, X. Dai, J. Zhao, D. He, G. Li, B. Wang, and X. Cui, *Catalytic Activity Enhancement on Alcohol Dehydrogenation via Directing Reaction Pathways from Single- to Double-Atom Catalysis*, J. Am. Chem. Soc. **144**, 4913 (2022).
 - [35] Y. Wang, B. J. Park, V. K. Paidi, R. Huang, Y. Lee, K.-J. Noh, K.-S. Lee, and J. W. Han, *Precisely Constructing Orbital Coupling-Modulated Dual-Atom Fe Pair Sites for Synergistic CO₂ Electroreduction*, ACS Energy Lett. **7**, 640 (2022).
 - [36] N. Karmodak, S. Vijay, G. Kastlunger, and K. Chan, *Computational Screening of Single and Di-Atom Catalysts for Electrochemical CO₂ Reduction*, ACS Catal. **12**, 4818 (2022).
 - [37] J. Hao, Z. Zhuang, J. Hao, C. Wang, S. Lu, F. Duan, F. Xu, M. Du, and H. Zhu, *Interatomic Electronegativity Offset Dictates Selectivity When Catalyzing the CO₂ Reduction Reaction*, Adv. Energy Mater. **12**, 2200579 (2022).
 - [38] F. Li and Q. Tang, *Understanding Trends in the Activity and Selectivity of Bi-Atom Catalysts for the Electrochemical Reduction of Carbon Dioxide*, J. Mater. Chem. A **9**, 8761 (2021).
 - [39] T. Ding, X. Liu, Z. Tao, T. Liu, T. Chen, W. Zhang, X. Shen, D. Liu, S. Wang, and B. Pang et al., *Atomically Precise Dinuclear Site Active toward Electrocatalytic CO₂ Reduction*, J. Am. Chem. Soc. **143**, 11317 (2021).
 - [40] B. Qiao, A. Wang, X. Yang, L. F. Allard, Z. Jiang, Y. Cui, J. Liu, J. Li, and T. Zhang, *Single-Atom Catalysis of CO Oxidation Using Pt₁/FeO_x*, Nat. Chem. **3**, 634 (2011).
 - [41] P. Liu, Y. Zhao, R. Qin, S. Mo, G. Chen, L. Gu, D. M. Chevrier, P. Zhang, Q. Guo, and D. Zang et al., *Photochemical Route for Synthesizing Atomically Dispersed Palladium Catalysts*, Science **352**, 797 (2016).
 - [42] J.-C. Liu, H. Xiao, and J. Li, *Constructing High-Loading Single-Atom/Cluster Catalysts via an Electrochemical Potential Window Strategy*, J. Am. Chem. Soc. **142**, 3375 (2020).
 - [43] Y. Li, W. Shan, M. J. Zachman, M. Wang, S. Hwang, H. Tabassum, J. Yang, X. Yang, S. Karakalos, and Z. Feng et al., *Atomically Dispersed Dual-Metal Site Catalysts for Enhanced CO₂ Reduction: Mechanistic Insight into Active Site Structures*, Angew. Chem. Internat. Edit. **61**, e202205632 (2022).
 - [44] L. Zhao, Y. Zhang, L.-B. Huang, X.-Z. Liu, Q.-H. Zhang, C. He, Z.-Y. Wu, L.-J. Zhang, J. Wu, and W. Yang et al., *Cascade Anchoring Strategy for General Mass Production of High-Loading Single-Atomic Metal-Nitrogen Catalysts*, Nat. Commun. **10**, 1278 (2019).
 - [45] C. Tang, Y. Jiao, B. Shi, J.-N. Liu, Z. Xie, X. Chen, Q. Zhang, and S.-Z. Qiao, *Coordination Tunes Selectivity: Two-Electron Oxygen Reduction on High-Loading Molybdenum Single-*

- Atom Catalysts*, Angew. Chem. Internat. Edit. **59**, 9171 (2020).
- [46] S. Tian, C. Peng, J. Dong, Q. Xu, Z. Chen, D. Zhai, Y. Wang, L. Gu, P. Hu, and H. Duan et al., *High-Loading Single-Atomic-Site Silver Catalysts with an $\text{Ag}_1\text{-C}_2\text{N}_1$ Structure Showing Superior Performance for Epoxidation of Styrene*, ACS Catal. **11**, 4946 (2021).
- [47] J. Li, W. Xia, J. Tang, Y. Gao, C. Jiang, Y. Jia, T. Chen, Z. Hou, R. Qi, and D. Jiang et al., *Metal–Organic Framework-Derived Graphene Mesh: A Robust Scaffold for Highly Exposed Fe-N_4 Active Sites toward an Excellent Oxygen Reduction Catalyst in Acid Media*, J. Am. Chem. Soc. **144**, 9280 (2022).
- [48] Y. Xiong, W. Sun, P. Xin, W. Chen, X. Zheng, W. Yan, L. Zheng, J. Dong, J. Zhang, and D. Wang et al., *Gram-Scale Synthesis of High-Loading Single-Atomic-Site Fe Catalysts for Effective Epoxidation of Styrene*, Adv. Mater. **32**, 2000896 (2020).
- [49] Y. Zhou, X. Tao, G. Chen, R. Lu, D. Wang, M.-X. Chen, E. Jin, J. Yang, H.-W. Liang, and Y. Zhao et al., *Multilayer Stabilization for Fabricating High-Loading Single-Atom Catalysts*, Nat. Commun. **11**, 5892 (2020).
- [50] X. Hai, S. Xi, S. Mitchell, K. Harrath, H. Xu, D. F. Akl, D. Kong, J. Li, Z. Li, and T. Sun et al., *Scalable Two-Step Annealing Method for Preparing Ultra-High-Density Single-Atom Catalyst Libraries*, Nat. Nanotech. **17**, 174 (2022).
- [51] C. Xia, Y. Qiu, Y. Xia, P. Zhu, G. King, X. Zhang, Z. Wu, J. Y. (Timothy) Kim, D. A. Cullen, and D. Zheng et al., *General Synthesis of Single-Atom Catalysts with High Metal Loading Using Graphene Quantum Dots*, Nat. Chem. **13**, 887 (2021).
- [52] J. P. Perdew, K. Burke, and M. Ernzerhof, *Generalized Gradient Approximation Made Simple*, Phys. Rev. Lett. **77**, 3865 (1996).
- [53] G. Kresse and J. Furthmüller, *Efficient Iterative Schemes for Ab Initio Total-Energy Calculations Using a Plane-Wave Basis Set*, Phys. Rev. B **54**, 11169 (1996).
- [54] G. Kresse and J. Furthmüller, *Efficiency of Ab-Initio Total Energy Calculations for Metals and Semiconductors Using a Plane-Wave Basis Set*, Com. Mater. Sci. **6**, 15 (1996).
- [55] S. Grimme, J. Antony, S. Ehrlich, and H. Krieg, *A Consistent and Accurate Ab Initio Parametrization of Density Functional Dispersion Correction (DFT-D) for the 94 Elements H-Pu*, J. Chem. Phys. **132**, 154104 (2010).
- [56] A. Togo, F. Oba, and I. Tanaka, *First-Principles Calculations of the Ferroelastic Transition between Rutile-Type and CaCl_2 -Type SiO_2 at High Pressures*, Phys. Rev. B **78**, 134106 (2008).
- [57] J. Tersoff and D. R. Hamann, *Theory and Application for the Scanning Tunneling Microscope*, Phys. Rev. Lett. **50**, 1998 (1983).
- [58] J. Greeley and J. K. Nørskov, *Electrochemical Dissolution of Surface Alloys in Acids: Thermodynamic Trends from First-Principles Calculations*, Electrochim. Acta **52**, 5829 (2007).
- [59] X. Guo, S. Lin, J. Gu, S. Zhang, Z. Chen, and S. Huang, *Simultaneously Achieving High Activity and Selectivity toward Two-Electron O_2 Electroreduction: The Power of Single-Atom Catalysts*, ACS Catal. **9**, 11042 (2019).
- [60] X. Lv, W. Wei, B. Huang, Y. Dai, and T. Frauenheim, *High-Throughput Screening of Synergistic Transition Metal Dual-Atom Catalysts for Efficient Nitrogen Fixation*, Nano Lett. **21**, 1871 (2021).
- [61] Q. Wei and X. Peng, *Superior Mechanical Flexibility of Phosphorene and Few-Layer Black Phosphorus*, Appl. Phys. Lett. **104**, 251915 (2014).

- [62] A. A. Peterson, F. Abild-Pedersen, F. Studt, J. Rossmeisl, and J. K. Nørskov, *How Copper Catalyzes the Electroreduction of Carbon Dioxide into Hydrocarbon Fuels*, *Energy Environ. Sci.* **3**, 1311 (2010).
- [63] J. K. Nørskov, J. Rossmeisl, A. Logadottir, L. Lindqvist, J. R. Kitchin, T. Bligaard, and H. Jónsson, *Origin of the Overpotential for Oxygen Reduction at a Fuel-Cell Cathode*, *J. Phys. Chem. B* **108**, 17886 (2004).
- [64] J. Rossmeisl, A. Logadottir, and J. K. Nørskov, *Electrolysis of Water on (Oxidized) Metal Surfaces*, *Chem. Phys.* **319**, 178 (2005).
- [65] <http://Webbook.Nist.Gov/Chemistry/>, (n.d.).
- [66] V. Wang, N. Xu, J.-C. Liu, G. Tang, and W.-T. Geng, *VASPKIT: A User-Friendly Interface Facilitating High-Throughput Computing and Analysis Using VASP Code*, *Comp. Phys. Commun.* **267**, 108033 (2021).
- [67] K. Mathew, R. Sundararaman, K. Letchworth-Weaver, T. A. Arias, and R. G. Hennig, *Implicit Solvation Model for Density-Functional Study of Nanocrystal Surfaces and Reaction Pathways*, *J. Chem. Phys.* **140**, 084106 (2014).
- [68] G. Xiao, R. Lu, J. Liu, X. Liao, Z. Wang, and Y. Zhao, *Coordination Environments Tune the Activity of Oxygen Catalysis on Single Atom Catalysts: A Computational Study*, *Nano Res.* **15**, 3073 (2022).
- [69] S. Plimpton, *Fast Parallel Algorithms for Short-Range Molecular Dynamics*, *J Comput. Phys.* **117**, 1 (1995).
- [70] W. L. Jorgensen, J. Chandrasekhar, J. D. Madura, R. W. Impey, and M. L. Klein, *Comparison of Simple Potential Functions for Simulating Liquid Water*, *J. Chem. Phys.* **79**, 926 (1983).
- [71] M. Reda, H. A. Hansen, and T. Vegge, *DFT Study of Stabilization Effects on N-Doped Graphene for ORR Catalysis*, *Catal Today* **312**, 118 (2018).
- [72] T. Jing, T. Li, D. Rao, M. Wang, and Y. Zuo, *Defining the Loading of Single-Atom Catalysts: Weight Fraction or Atomic Fraction?*, *Mater. Today Energy* **31**, 101197 (2023).
- [73] J. Ibaceta-Jaña, R. Muydinov, P. Rosado, H. Mirhosseini, M. Chugh, O. Nazarenko, D. N. Dirin, D. Heinrich, M. R. Wagner, and T. D. Kühne et al., *Vibrational Dynamics in Lead Halide Hybrid Perovskites Investigated by Raman Spectroscopy*, *Phys. Chem. Chem. Phys.* **22**, 5604 (2020).
- [74] Y. Le Page and P. Saxe, *Symmetry-General Least-Squares Extraction of Elastic Data for Strained Materials from Ab Initio Calculations of Stress*, *Phys. Rev. B* **65**, 104104 (2002).
- [75] F. Liu, P. Ming, and J. Li, *Ab Initio Calculation of Ideal Strength and Phonon Instability of Graphene under Tension*, *Phys. Rev. B* **76**, 064120 (2007).
- [76] F. Mouhat and F.-X. Coudert, *Necessary and Sufficient Elastic Stability Conditions in Various Crystal Systems*, *Phys. Rev. B* **90**, 224104 (2014).
- [77] P. Lv, G. Tang, C. Yang, J. Deng, Y. Liu, X. Wang, X. Wang, and J. Hong, *Half-Metallicity in Two-Dimensional Co₂Se₃ Monolayer with Superior Mechanical Flexibility*, *2D Mater* **5**, 045026 (2018).
- [78] C. Lee, X. Wei, J. W. Kysar, and J. Hone, *Measurement of the Elastic Properties and Intrinsic Strength of Monolayer Graphene*, *Science* **321**, 385 (2008).
- [79] Y. Yang, Y. Xue, H. Zhang, and H. Chang, *Flexible H₂O₂ Microfluidic Fuel Cell Using Graphene/Prussian Blue Catalyst for High Performance*, *Chem. Eng. J* **369**, 813 (2019).
- [80] X. Guo, J. Gu, S. Lin, S. Zhang, Z. Chen, and S. Huang, *Tackling the Activity and Selectivity*

- Challenges of Electrocatalysts toward the Nitrogen Reduction Reaction via Atomically Dispersed Biatom Catalysts*, J. Am. Chem. Soc. **142**, 5709 (2020).
- [81] D. Ma, Y. Wang, L. Liu, and Y. Jia, *Electrocatalytic Nitrogen Reduction on the Transition-Metal Dimer Anchored N-Doped Graphene: Performance Prediction and Synergetic Effect*, Phys. Chem. Chem. Phys. **23**, 4018 (2021).
- [82] P. Lv, D. Wu, B. He, X. Li, R. Zhu, G. Tang, Z. Lu, D. Ma, and Y. Jia, *An Efficient Screening Strategy towards Multifunctional Catalysts for the Simultaneous Electroreduction of NO_3^- , NO_2^- and NO to NH_3* , J. Mater. Chem. A **10**, 9707 (2022).
- [83] J. Paier, M. Marsman, K. Hummer, G. Kresse, I. C. Gerber, and J. G. Ángyán, *Screened Hybrid Density Functionals Applied to Solids*, J. Chem. Phys. **124**, 154709 (2006).
- [84] L. Li, B. Huang, X. Tang, Y. Hong, W. Zhai, T. Hu, K. Yuan, and Y. Chen, *Recent Developments of Microenvironment Engineering of Single-Atom Catalysts for Oxygen Reduction toward Desired Activity and Selectivity*, Adv. Funct. Mater. **31**, 2103857 (2021).
- [85] Z. Qin and J. Zhao, *1 T-MoSe₂ Monolayer Supported Single Pd Atom as a Highly-Efficient Bifunctional Catalyst for ORR/OER*, J. Colloid Interf. Sci. **605**, 155 (2022).
- [86] L. Yu, F. Li, J. Zhao, and Z. Chen, *Revisiting Catalytic Performance of Supported Metal Dimers for Oxygen Reduction Reaction via Magnetic Coupling from First Principles*, Adv. Powder Mater. **1**, 100031 (2022).
- [87] D. Wu, B. He, Y. Wang, P. Lv, D. Ma, and Y. Jia, *Double-Atom Catalysts for Energy-Related Electrocatalysis Applications: A Theoretical Perspective*, J Phys. D Appl. Phys. **55**, 203001 (2022).
- [88] C. H. Choi, H.-K. Lim, M. W. Chung, J. C. Park, H. Shin, H. Kim, and S. I. Woo, *Long-Range Electron Transfer over Graphene-Based Catalyst for High-Performing Oxygen Reduction Reactions: Importance of Size, N-Doping, and Metallic Impurities*, J. Am. Chem. Soc. **136**, 9070 (2014).
- [89] H. Li, Z. Zhao, Q. Cai, L. Yin, and J. Zhao, *Nitrogen Electroreduction Performance of Transition Metal Dimers Embedded into N-Doped Graphene: A Theoretical Prediction*, J. Mater. Chem. A **8**, 4533 (2020).
- [90] S. Wang, L. Shi, X. Bai, Q. Li, C. Ling, and J. Wang, *Highly Efficient Photo-/Electrocatalytic Reduction of Nitrogen into Ammonia by Dual-Metal Sites*, ACS Cent. Sci. **6**, 1762 (2020).
- [91] Y. Ouyang, L. Shi, X. Bai, Q. Li, and J. Wang, *Breaking Scaling Relations for Efficient CO₂ Electrochemical Reduction through Dual-Atom Catalysts*, Chem. Sci. **11**, 1807 (2020).
- [92] H. A. Hansen, J. Rossmeisl, and J. K. Nørskov, *Surface Pourbaix Diagrams and Oxygen Reduction Activity of Pt, Ag and Ni(111) Surfaces Studied by DFT*, Phys. Chem. Chem. Phys. **10**, 3722 (2008).
- [93] W. Zhong, Y. Qiu, H. Shen, X. Wang, J. Yuan, C. Jia, S. Bi, and J. Jiang, *Electronic Spin Moment As a Catalytic Descriptor for Fe Single-Atom Catalysts Supported on C₂N*, J. Am. Chem. Soc. **143**, 4405 (2021).
- [94] R. Wang, L. Zhang, J. Shan, Y. Yang, J.-F. Lee, T.-Y. Chen, J. Mao, Y. Zhao, L. Yang, and Z. Hu et al., *Tuning Fe Spin Moment in Fe–N–C Catalysts to Climb the Activity Volcano via a Local Geometric Distortion Strategy*, Adv. Sci. **9**, 2203917 (2022).
- [95] Z. Duan and G. Henkelman, *Surface Charge and Electrostatic Spin Crossover Effects in CoN₄ Electrocatalysts*, ACS Catal. **10**, 12148 (2020).

Figures

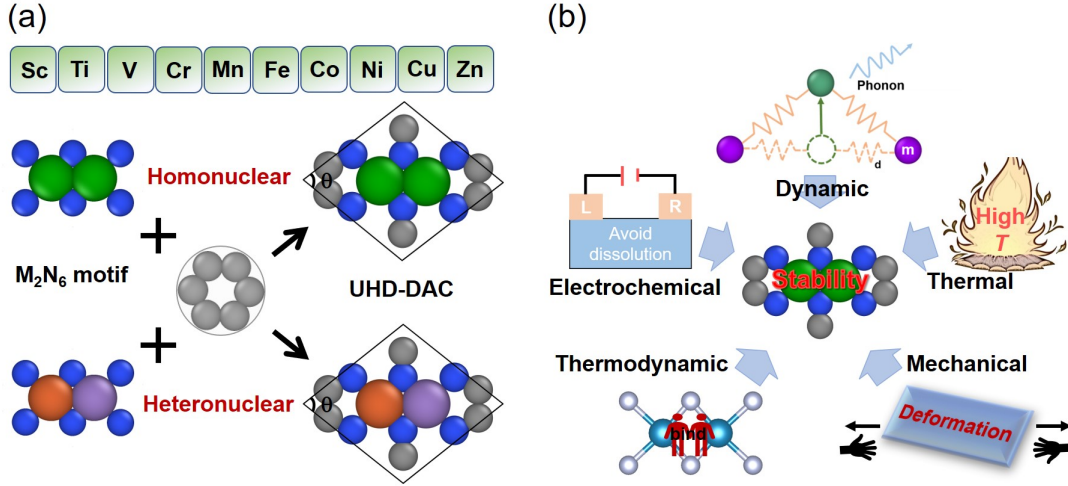


FIG. 1. (a) The schematic depiction of M_2N_6 UHD-DACs construction ($M = \text{Sc, Ti, V, Cr, Mn, Fe, Co, Ni, Cu, and Zn}$) from experimental M_2N_6 motif with the bonding of carbon atoms, including the homonuclear and heteronuclear DACs. (b) Five considered stabilities for M_2N_6 UHD-DACs: dynamic, thermal, mechanical, thermodynamic, and electrochemical stabilities.

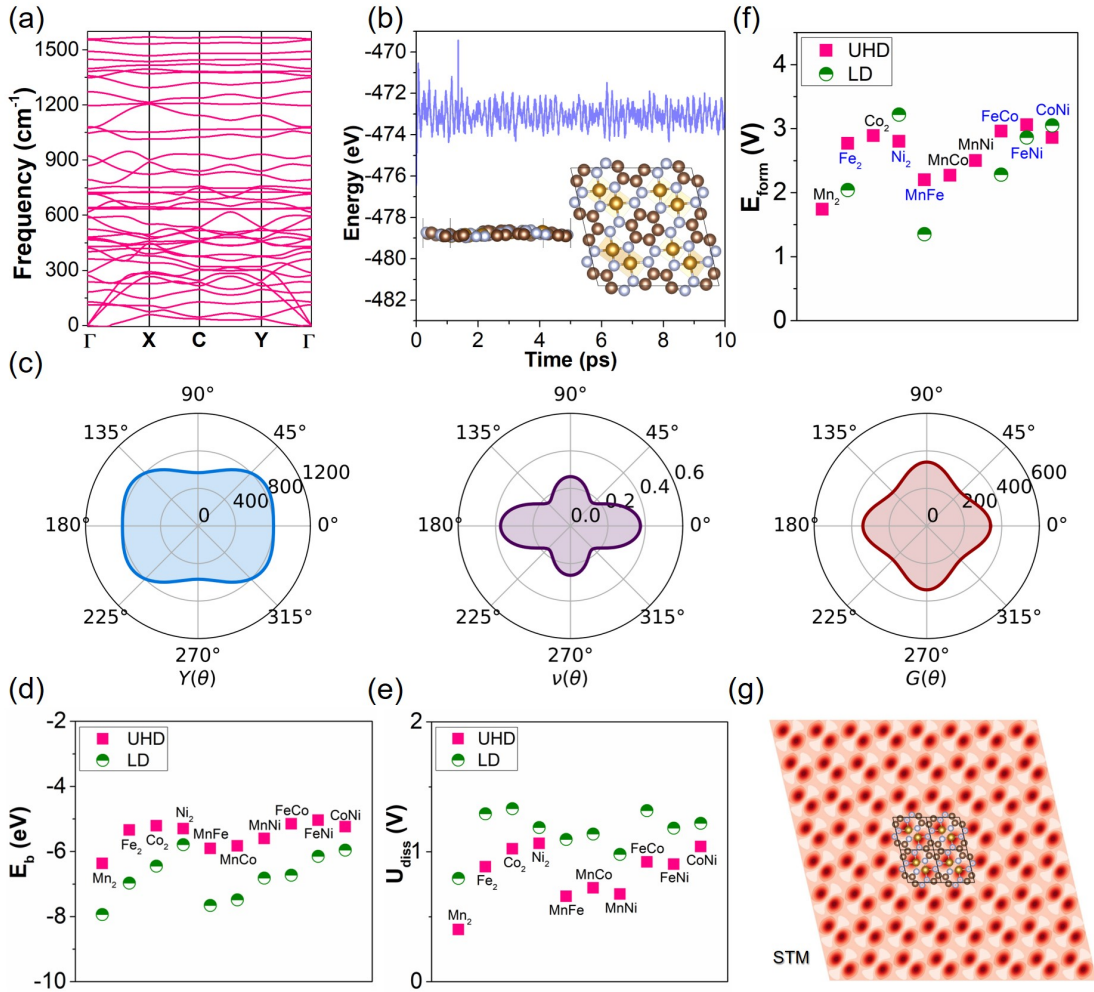


FIG. 2. (a) Phonon dispersions and (b) total free energy fluctuation during the AIMD

simulations for Fe₂N₆ UHD-DAC. In (b), The AIMD simulation was performed under 500 K for 10 ps with a time-step of 2 fs. The side and top views of the atomic configuration at 10 ps are shown as insets. (c) The 2D projection in polar coordinates of the Young's modulus (Y , GPa), Poisson's ratio (ν), and shear modulus (G) of Fe₂N₆ UHD-DAC. (d) Binding energies (E_b) and (e) dissolution potentials (U_{diss}) of double metal atoms for ten considerable M₂N₆ UHD-DACs with dynamic stability and their corresponding LD-DACs. (f) Formation energies (E_{form}) for ten considerable M₂N₆ UHD-DACs with dynamic stability and some corresponding experimental LD-DACs. (g) The simulated STM image for Fe₂N₆ UHD-DAC with the bias voltage of 1.0 V for the size of for 8×8 supercells. The tip was considered to be separated from the sample by a vacuum barrier width of 3.5 Å.

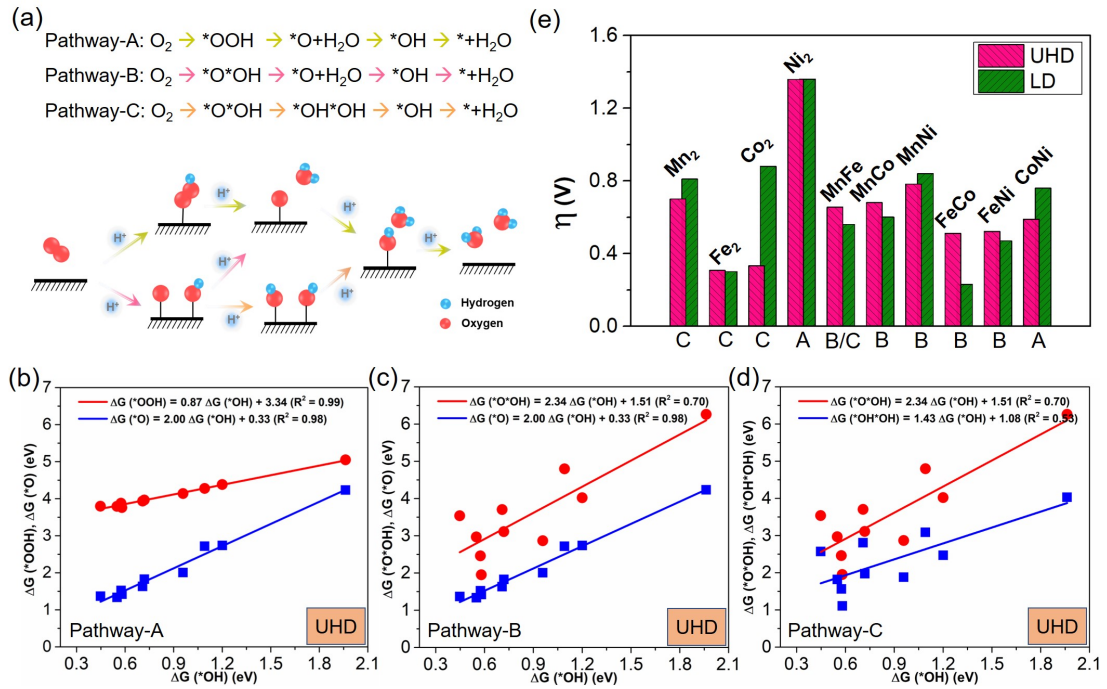


FIG. 3. (a) The schematic depiction of the three possible reaction pathways for the ORR at pH = 0. The scaling relationship between the Gibbs adsorption free energy of the oxygenated intermediates for (b) pathway-A, (c) pathway-B, and (d) pathway-C over the corresponding UHD-DACs. (e) The overpotentials (η_{ORR}) of ORR through the optimal reaction pathway (A, B or C) over corresponding UHD- and LD-DACs.

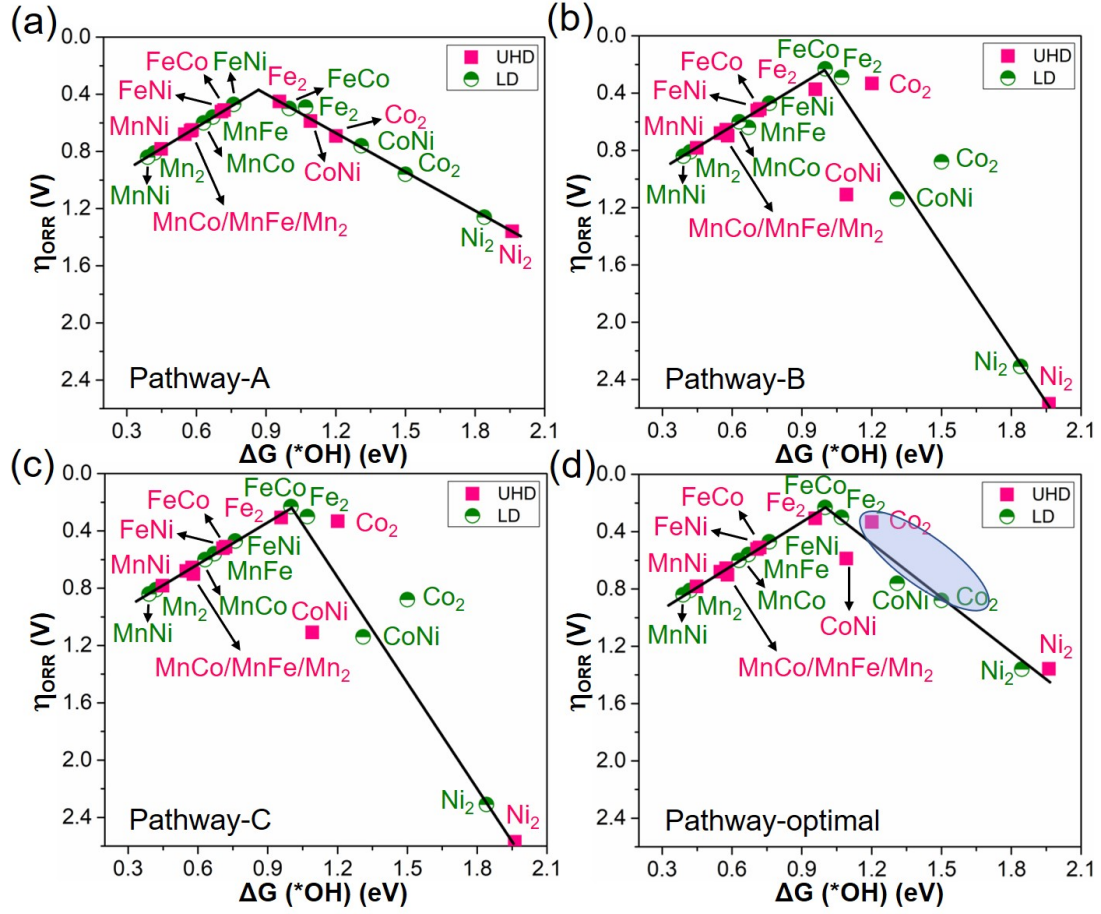


FIG. 4. Volcano plots for the η_{ORR} as a function of the Gibbs adsorption free energy $\Delta G (*\text{OH})$ for (a) pathway-A, (b) pathway-B, (c) pathway-C, and (d) optimal pathway. The pink and green marks represent the UHD- and LD-DACs, respectively.

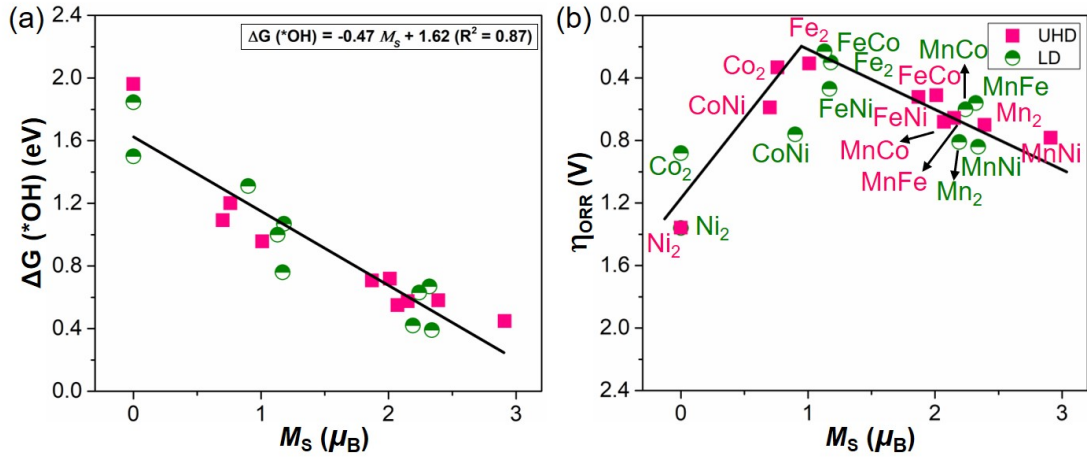


FIG. 5. (a) The scaling relationship between the Gibbs adsorption free energy of $*\text{OH}$ ($\Delta G (*\text{OH})$) in optimal pathway and the local spin magnetic moments (M_s) for the metal atom that anchor the $*\text{OH}$. (b) The volcano plots for the η_{ORR} for optimal pathway as a function of the local spin magnetic moments for the metal atom that anchor the $*\text{OH}$. The pink and green marks represent the UHD- and LD-DACs, respectively.

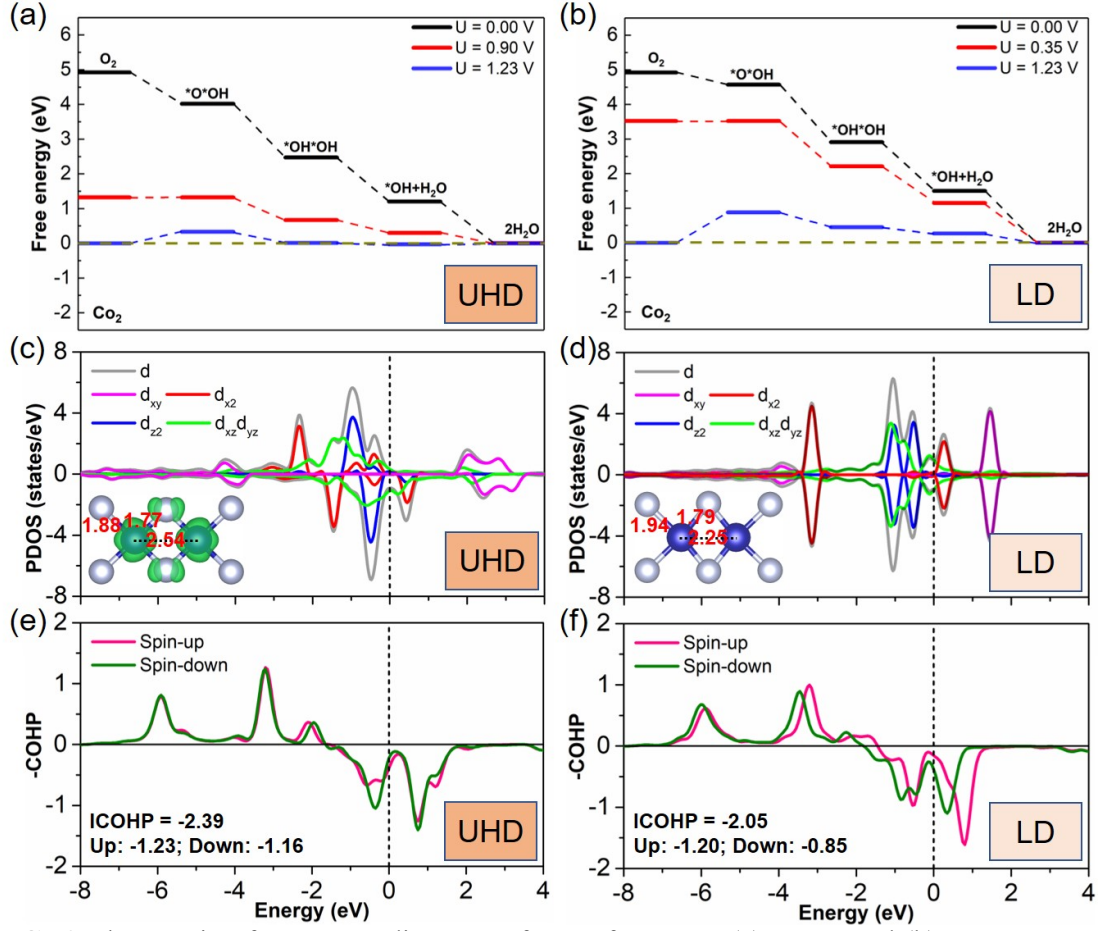


FIG. 6. The reaction free energy diagrams of ORR for Co_2N_6 (a) UHD- and (b) LD-DACs at different potentials for optimal pathway-C. The PDOS of Co 3d orbitals for Co_2N_6 (c) UHD- and (d) LD-DACs without $^*\text{OH}$ adsorption. Here the Fermi level was set to 0. The insert figure is the corresponding spin density (0.005 e/bohr^3) for Co_2N_6 UHD- and LD-DACs. The COHP for the interaction between Co and $^*\text{OH}$ for (e) UHD- and (f) LD-DACs.

Supplemental Material for
“Ultra-high-density double-atom catalyst with spin moment as activity descriptor for
oxygen reduction reaction”

Peng Lv¹, Wenjing Lv¹, Donghai Wu¹, Gang Tang², Xunwang Yan³, Zhansheng Lu^{4*},
Dongwei Ma^{1*}

¹*Key Laboratory for Special Functional Materials of Ministry of Education, and School of
Materials Science and Engineering, Henan University, Kaifeng 475004, China*

²*Advanced Research Institute of Multidisciplinary Science, Beijing Institute of Technology,
Beijing 100081, China*

³*College of Physics and Engineering, Qufu Normal University, Qufu 273165, China*

⁴*School of Physics, Henan Normal University, Xinxiang 453007, China*

* Corresponding author. E-mail: madw@henu.edu.cn, dwmachina@126.com (DW. Ma);
zslu@htu.edu.cn (ZS. Lu)

Table S1. The structural parameters of UHD-DACs, including the lattice constants a ($=b$), the spin stable state (SSS) of ferromagnetic (FM), antiferromagnetic (AFM), ferrimagnetic (FiM), and nonmagnetic (NM), and the theoretical metal loading (ML, wt%).

UHD-DACs	a (Å)	θ (Å)	SSS	ML
Sc ₂	6.89	105.2	NM	36.5
Ti ₂	6.75	104.7	FM	38.0
V ₂	6.64	103.8	FM	39.5
Cr ₂	6.57	103.0	AFM	40.0
Mn ₂	6.53	103.5	AFM	41.3
Fe ₂	6.46	103.1	FM	41.7
Co ₂	6.48	104.9	FM	43.0
Ni ₂	6.51	106.3	NM	42.9
Cu ₂	6.59	106.1	FM	44.9
Zn ₂	6.70	106.0	NM	45.6
MnFe	6.49	103.3	FiM	41.5
MnCo	6.48	103.4	FM	42.2
MnNi	6.54	105.3	FM	42.1
FeCo	6.50	104.7	FM	42.4
FeNi	6.51	105.2	FM	42.3
CoNi	6.51	106.3	FM	43.0

Table S2. The spin magnetic moments (μ_B) of M1 and M2 in the UHD- and LD-DACs. The values without (with) parentheses are calculated from PBE (HSE06) functional. Due to the large calculations for HSE06 functional, we only focus on the Co₂N₆ DAC among the LD-DAC system.

System	ULD-DACs		LD-DACs	
	M1	M2	M1	M2
Mn ₂	2.36 (3.20)	-2.36 (-3.20)	2.39	-2.39
Fe ₂	1.03 (1.68)	1.03 (1.68)	1.11	1.11
Co ₂	0.75 (1.14)	0.75 (1.14)	0.00 (0.00)	0.00 (0.00)
Ni ₂	0.00 (0.00)	0.00 (0.00)	0.00	0.00
MnFe	2.33 (3.14)	-0.83 (-2.18)	2.32	-1.19
MnCo	2.09 (3.22)	-0.04 (-0.73)	2.24	-0.04
MnNi	2.92 (3.43)	0.05 (0.01)	2.22	0.01
FeCo	2.00 (2.39)	0.52 (1.02)	1.13	-0.02
FeNi	1.86 (2.41)	0.08 (0.02)	2.18	0.16
CoNi	0.69 (1.03)	0.00 (0.00)	0.90	0.17

Table S3. The mechanical properties of UHD-DACs, including the elastic constants C_{ij} (GPa), in-plane Young's modulus E_x and E_y (GPa), in-plane Poisson's ratio ν_{xy} and ν_{yx} , in-plane shear modulus G (GPa).

M_2	C_{11}	C_{22}	C_{12}	C_{66}	E_x	E_y	ν_{xy}	ν_{yx}	G
Mn ₂	894.61	629.46	235.31	340.41	806.65	567.57	0.37	0.26	340.41
Fe ₂	929.58	712.57	232.14	341.13	853.95	654.60	0.33	0.25	341.13
Co ₂	850.87	673.34	293.51	363.02	722.93	572.10	0.44	0.34	363.02
Ni ₂	829.60	733.99	264.77	365.75	734.10	649.49	0.36	0.32	365.75
MnFe	915.74	674.40	234.16	343.23	834.44	614.52	0.35	0.26	343.23
MnCo	915.69	688.81	242.73	339.40	830.15	624.47	0.35	0.27	339.40
MnNi	810.35	668.02	289.44	351.09	684.94	564.64	0.43	0.36	351.09
FeCo	851.50	653.41	293.94	357.65	719.27	551.94	0.45	0.35	357.65
FeNi	820.89	655.66	300.26	358.37	683.38	545.83	0.46	0.37	358.37
CoNi	828.65	735.04	262.32	365.08	735.03	652.00	0.36	0.32	365.08

Table S4. The binding energy (E_b), dissolution potential (U_{diss} , versus SHE), and formation energy (E_{form}) for considered UHD-DACs and their corresponding LD-DACs. It should be noted that this definition for E_b takes the metal bulk as the reference system while E_b' uses the free metal atom as reference. Experimental values for U_{diss}° (pH = 0) and N_e are taken from reference. [58,59] The E_{form} values marked by red color for LD-DACs are the experimentally synthesized systems.

DACs	E_b		E_b'		U_{diss}°	N_e	U_{diss}		E_{form}	
	UHD	LD	UHD	LD			UHD	LD	UHD	LD
Mn ₂	-6.37	-7.94	-14.65	-16.22	-1.19	2	0.40	0.79	1.74	1.07
Fe ₂	-5.34	-6.97	-16.28	-17.91	-0.45	2	0.88	1.29	2.77	2.04
Co ₂	-5.21	-6.45	-16.47	-17.71	-0.28	2	1.02	1.33	2.89	2.56
Ni ₂	-5.30	-5.79	-15.90	-16.39	-0.26	2	1.07	1.19	2.80	3.22
MnFe	-5.91	-7.66	-15.52	-17.27	-0.82	2	0.66	1.09	2.20	1.35
MnCo	-5.83	-7.49	-15.60	-17.26	-0.74	2	0.72	1.14	2.27	1.52
MnNi	-5.60	-6.82	-15.04	-16.26	-0.73	2	0.67	0.98	2.50	2.19
FeCo	-5.15	-6.73	-16.25	-17.83	-0.37	2	0.92	1.32	2.96	2.28
FeNi	-5.04	-6.15	-15.81	-16.92	-0.36	2	0.90	1.18	3.06	2.86
CoNi	-5.24	-5.96	-16.17	-16.89	-0.27	2	1.04	1.22	2.86	3.05

Table S5. The ΔG (*O), ΔG_1 (ORR), and ΔG (*H) on ten stable UHD-DACs.

UHD-DACs	ΔG (*O)	ΔG_1 (ORR)	ΔG (*H)
Mn ₂	1.42	-1.16	0.32
Fe ₂	2.01	-0.78	0.32
Co ₂	2.74	-0.54	0.48
Ni ₂	4.23	0.13	0.37
MnFe	1.52	-1.04	0.37
MnCo	1.34	-1.13	0.33
MnNi	1.37	-1.12	0.43
FeCo	1.83	-0.96	0.30
FeNi	1.63	-0.98	0.38
CoNi	2.72	-0.64	0.31

Herein, we have investigated the competitive reactions on the UHD-DACs, including the two-electron ORR and hydrogen evolution reaction (HER). For competitive two-electron ORR toward H₂O₂ production, the Gibbs free energy of *O (ΔG (*O)) for a catalyst with a high selectivity should be more positive than 3.52 eV. [59] Our results showed that the ΔG (*O) for most of the UHD-DACs are less than 3.52 eV, indicating their poor selectivity for two-electron ORR toward H₂O₂. Only one exception, *i.e.*, Ni₂N₆ UHD-DAC, has the larger ΔG (*O) with 4.23 eV, which indeed exhibits high two-electron ORR selectivity. Herein, we consider the four-electron ORR toward H₂O on Ni₂N₆ UHD-DAC with the aim to investigate the activity descriptor for all DAC systems. For competitive HER, we calculated the *H adsorption on various UHD-DACs and the comparison results of ΔG (*H) and ΔG_1 (ORR) (here $\Delta G_1 = \Delta G$ (*OOH) – 4.92)) are organized in **Table S5**. We found that all the UHD-DACs have the positive ΔG (*H) values but negative ΔG_1 (ORR) values, indicating that they have a strong ability to suppress the competing HER.

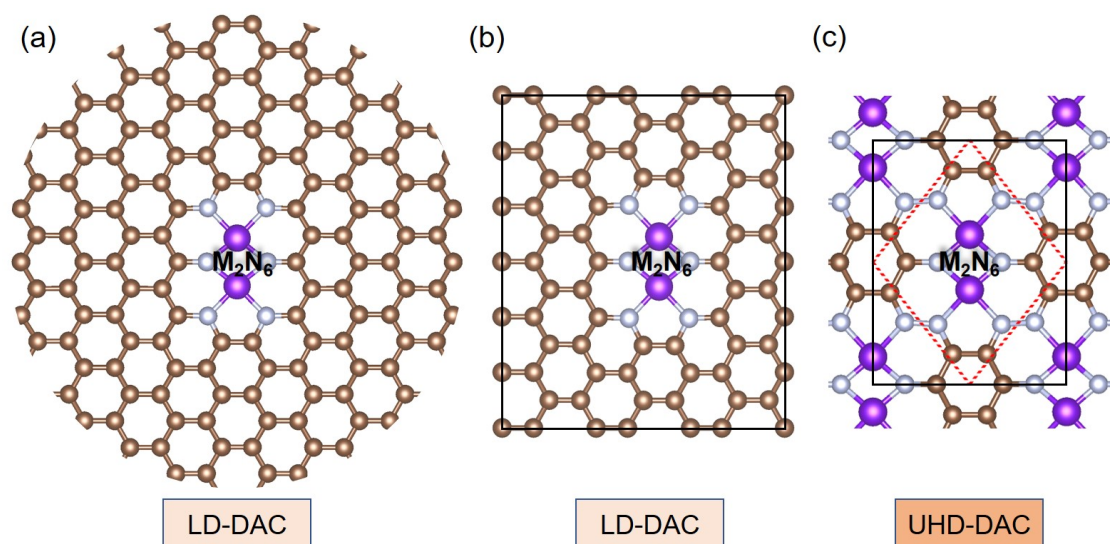


Fig. S1. (a) The atomic structure for experimental M_2N_6 LD-DAC with each transition-metal atom coordinated with four N atoms in carbon sheet (M_2N_6 with two MN_4 motifs). (b) For comparison with UHD-DAC, the theoretical model of experimentally synthesized LD-DACs with low metal contents is built by embedding the same M_2N_6 active center in 3×6 rectangular supercells. (c) The atomic structure for our constructed UHD-DAC. The red dash lines imply the primitive cell and the black solid lines denote the conventional cell. We can find our constructed UHD-DAC and experimentally prepared LD-DAC both have the same active center, *i.e.*, metal dimers with the same N coordination (M_2N_6 with two MN_4 motifs). The difference is that they contain different amounts of carbon in their substrate, resulting in different metal contents and densities of active site.

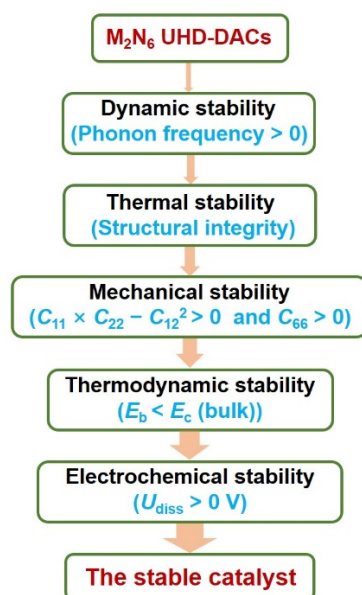


Fig. S2. The screening strategy with limiting criterion for the selection of stable UHD-DACs, including five aspects: dynamic, thermal, mechanical, thermodynamic, and electrochemical stabilities (**Fig. 1(b)**).

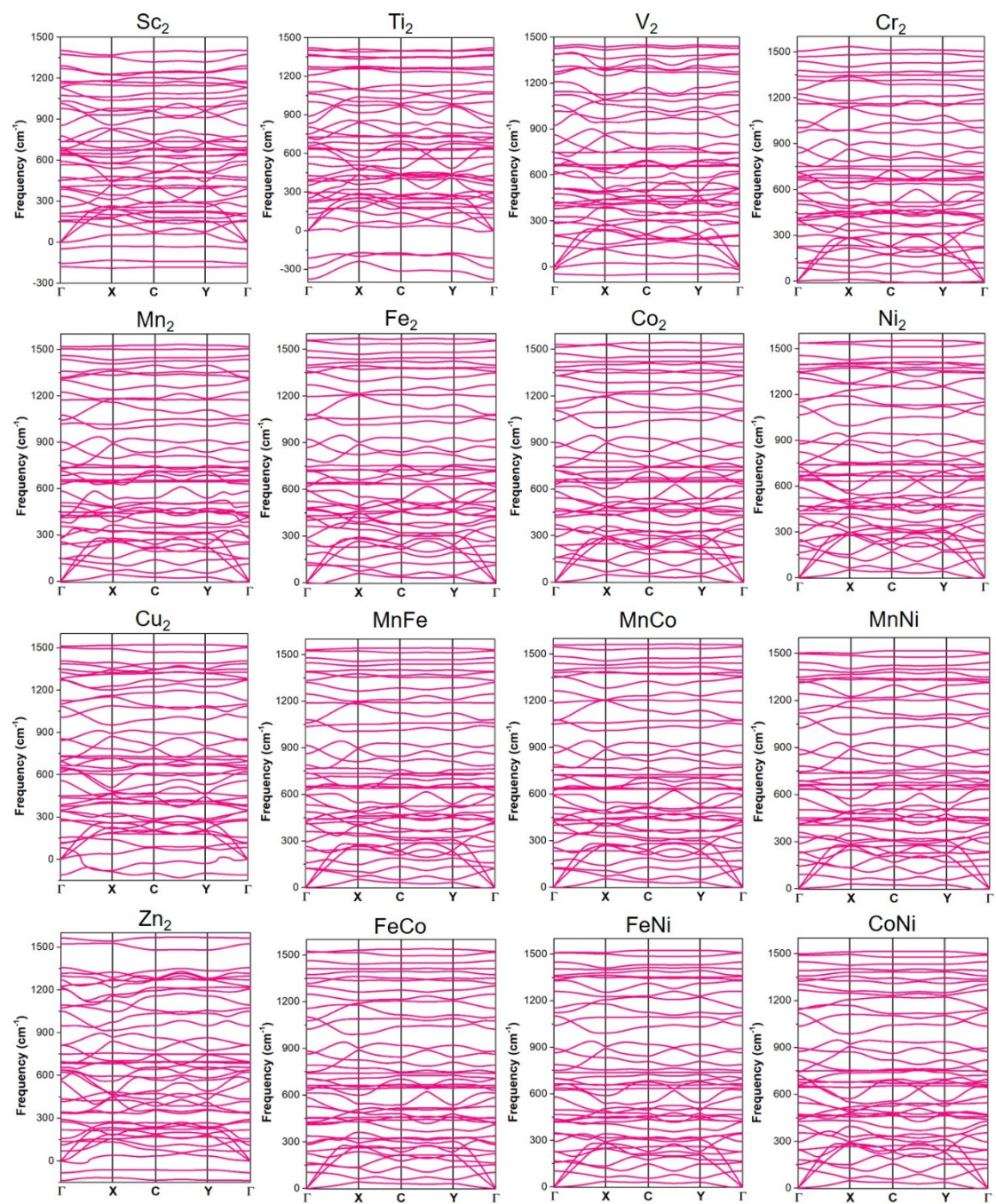


Fig. S3. The phonon dispersions of various UHD-DACs. The Fe_2N_6 case have also been shown in the **Fig. 2** of main text.

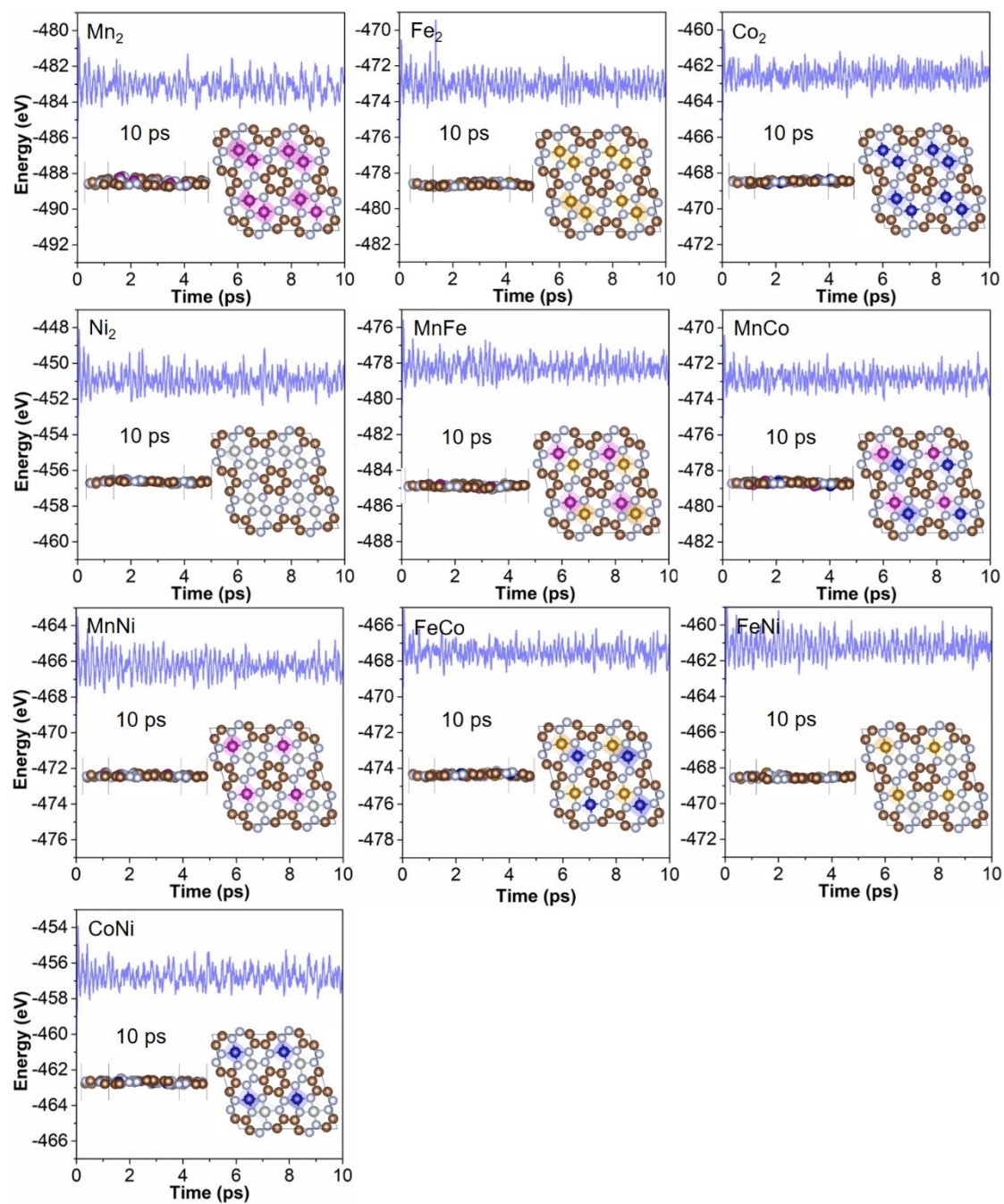


Fig. S4. The total free energy fluctuations of various UHD-DACs during the AIMD simulations at 500 K for 10 ps. The Fe_2N_6 case have also been shown in the **Fig. 2** of main text.

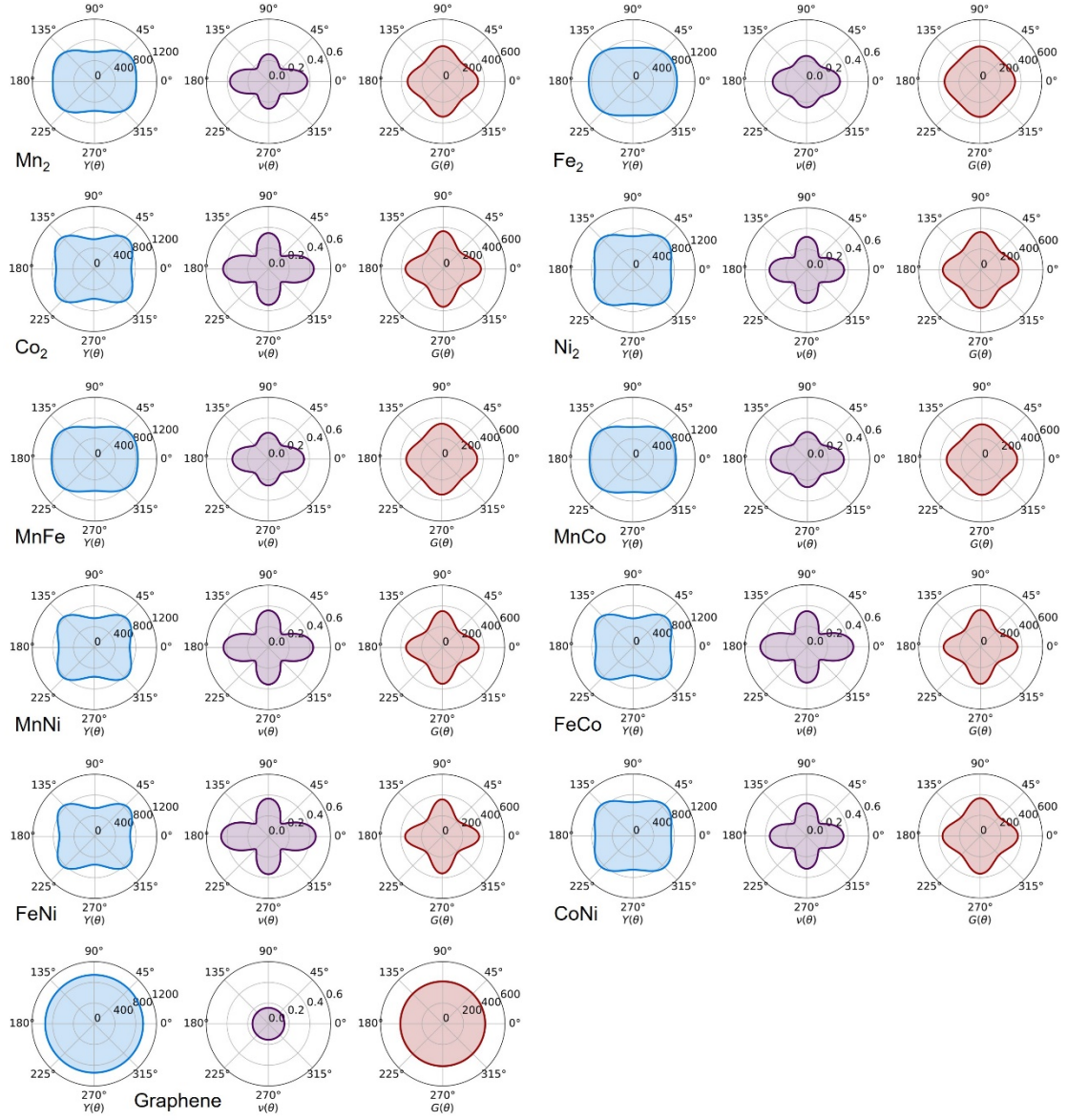


Fig. S5. The 2D projection in polar coordinates of the Young's modulus (Y , GPa), Poisson's ratio (ν), and shear modulus (G) of various UHD-DACs. The mechanical properties of graphene are also calculated for the comparison. The Fe_2N_6 case have also been shown in the **Fig. 2** of main text.

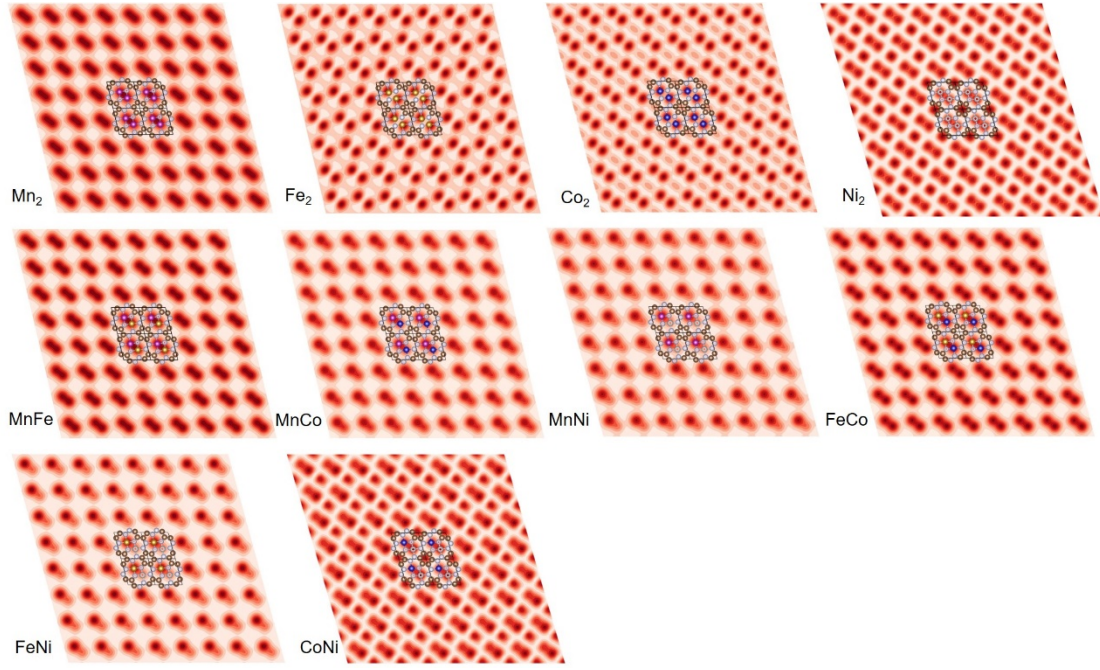


Fig. S6. The simulated STM images for the size of for 8×8 supercells with the different bias voltage (1.0 V for Mn_2N_6 , Fe_2N_6 , Co_2N_6 , Ni_2N_6 , and CoNiN_6 UHD-DACs, 2.0 V for MnFeN_6 , MnCoN_6 , and FeCoN_6 UHD-DACs, 3.0 V for MnNiN_6 and FeNiN_6 UHD-DACs). The tip was considered to be separated from the sample by a vacuum barrier width of 3.5 Å. The Fe_2N_6 case have also been shown in the **Fig. 2** of main text.

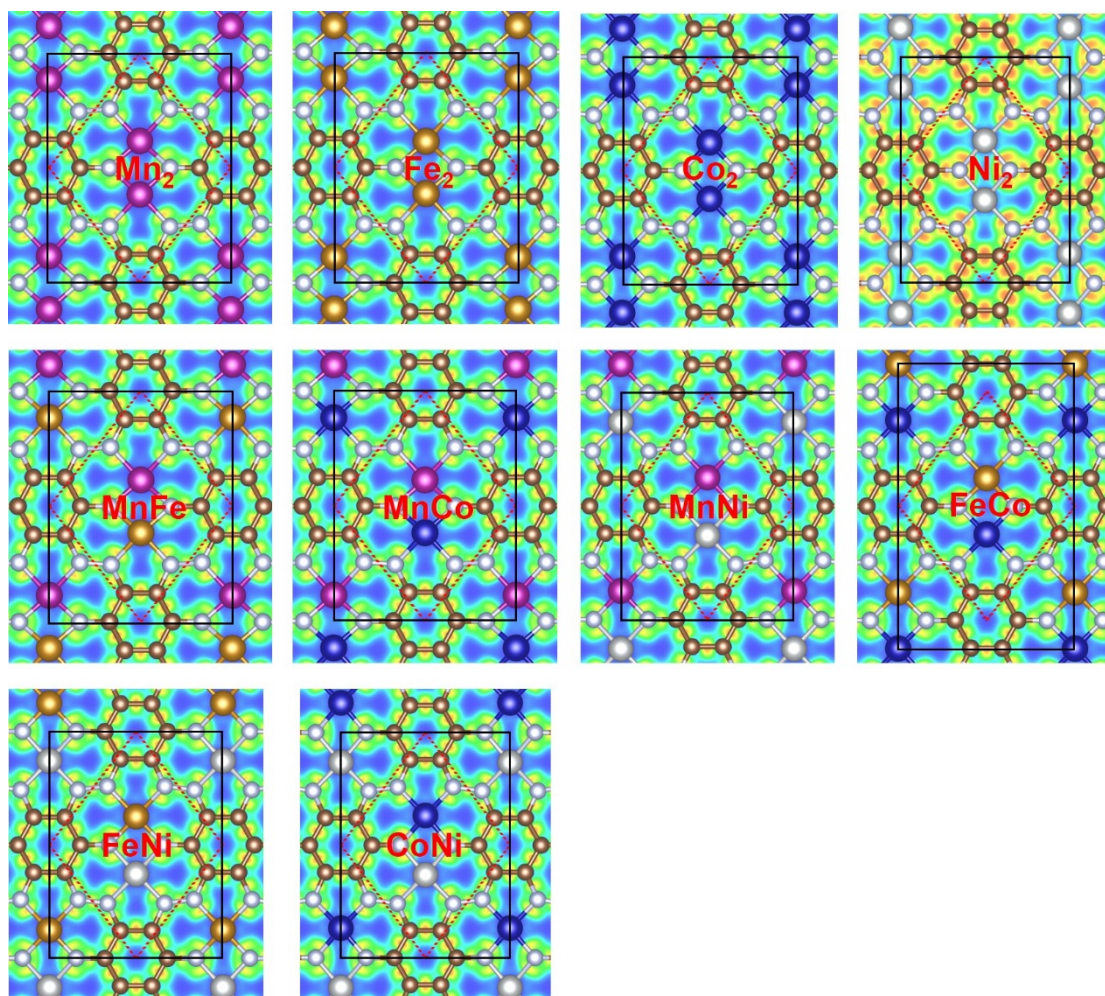


Fig. S7. The atomic structures with the planer-drawn electron localization function (ELF) of various UHD-DACs. The red dash lines imply the primitive cell and the black solid lines denote the conventional cell.

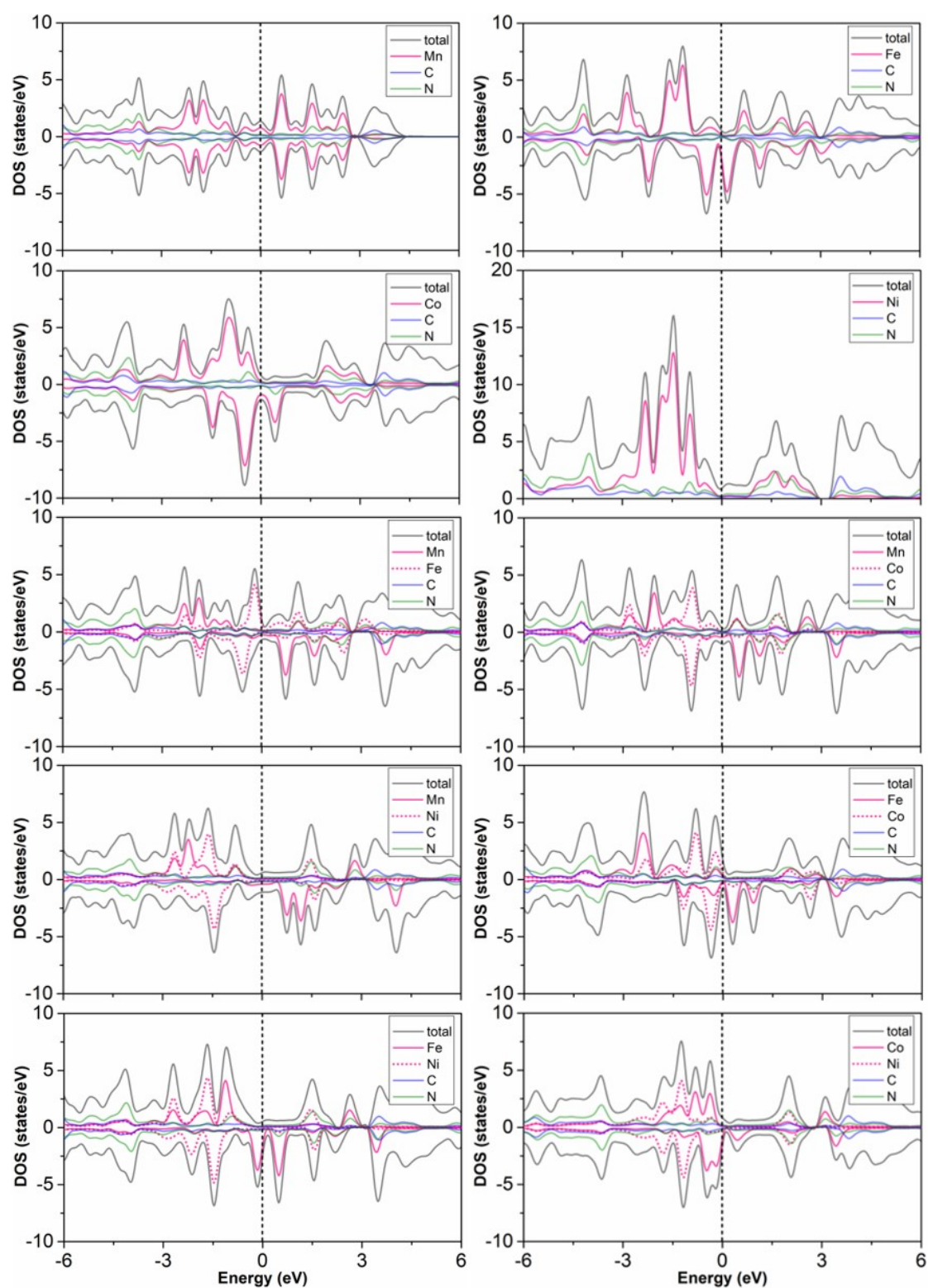


Fig. S8. The total density of states (TDOS), and partial density of states (PDOS) for various stable UHD-DACs based on GGA-PBE functional, respectively.

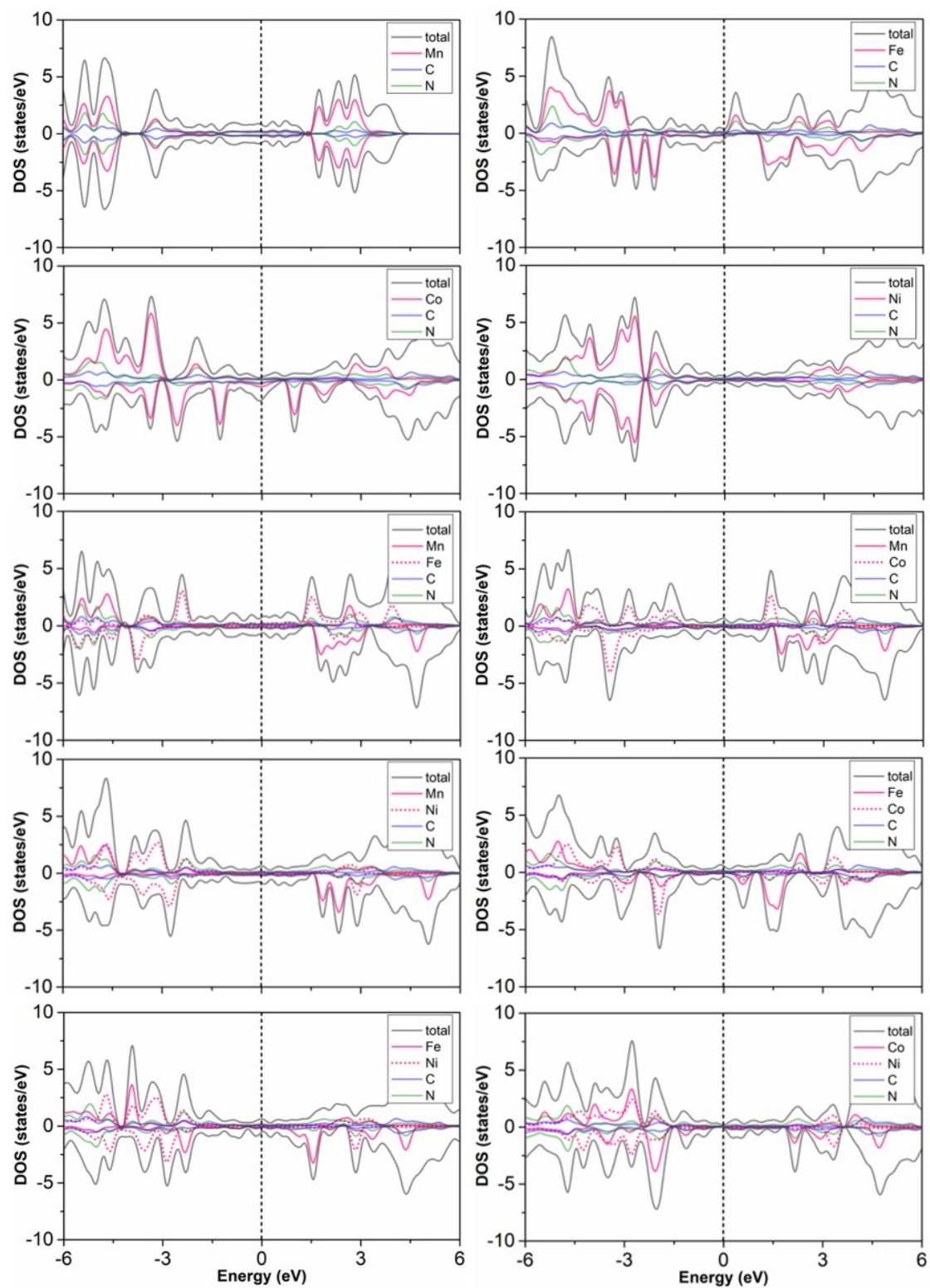


Fig. S9. The total density of states (TDOS), and partial density of states (PDOS) for various stable UHD-DACs based on HSE06 hybrid functional, respectively.

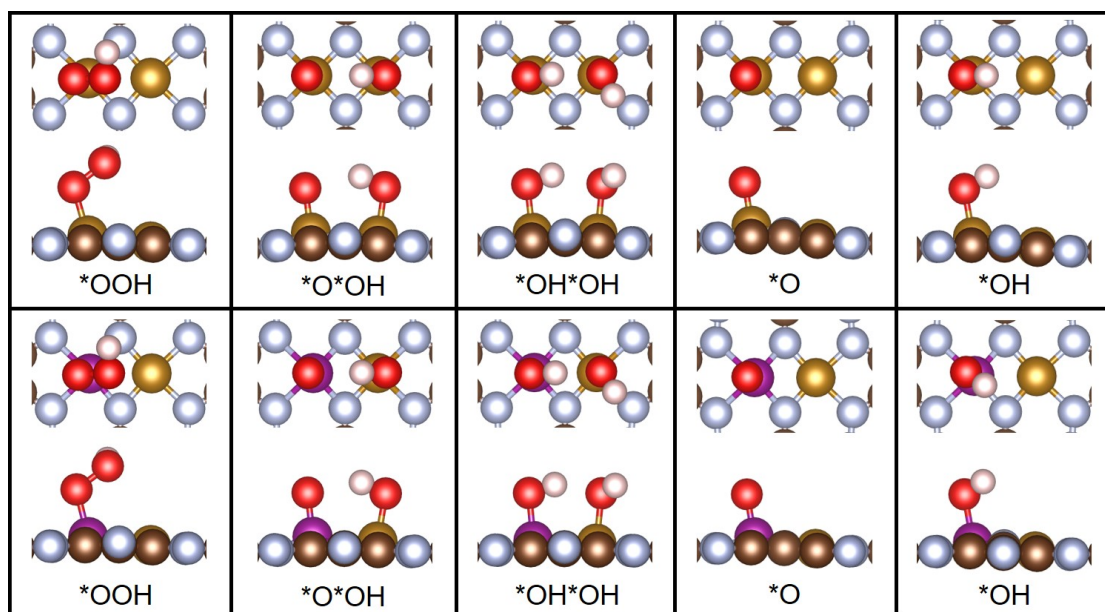


Fig. S10. The atomic configurations of *OOH, *O*OH, *OH*OH, *O, and *OH species on Fe₂N₆ and MnFeN₆ UHD-DACs, respectively. The other UHD- and LD-DACs have the same atomic configurations of oxygenated species.

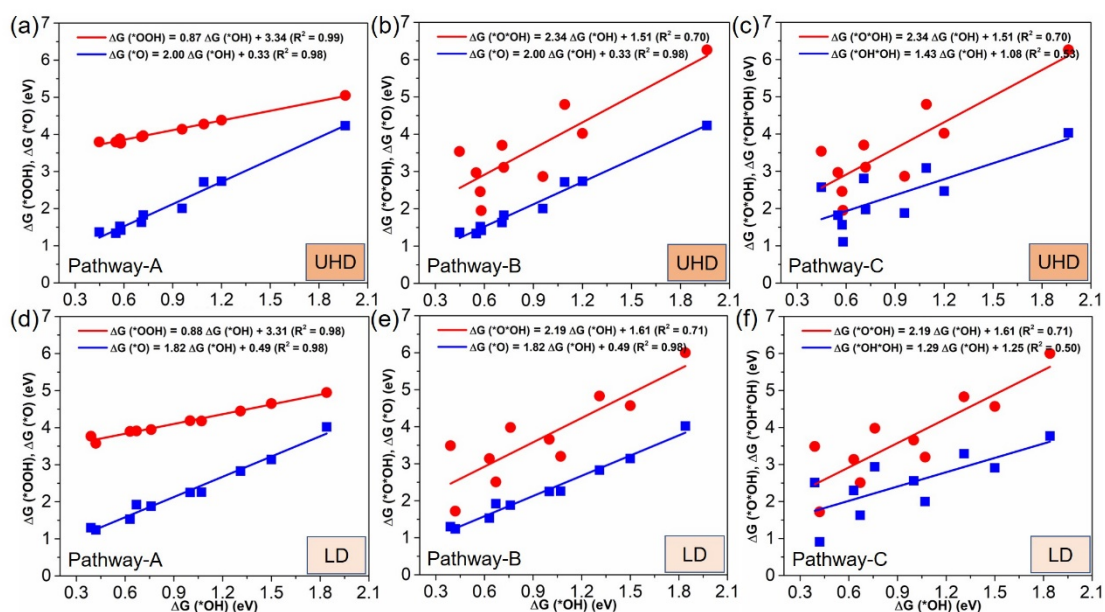


Fig. S11. The scaling relationship between the Gibbs adsorption free energy of the oxygenated intermediates for pathway-A, pathway-B, and pathway-C over the corresponding (a-c) UHD- and (d-f) LD-DACs, respectively. The scaling relationship for UHD-DACs are reprinted in the **Fig. 3** of main text.

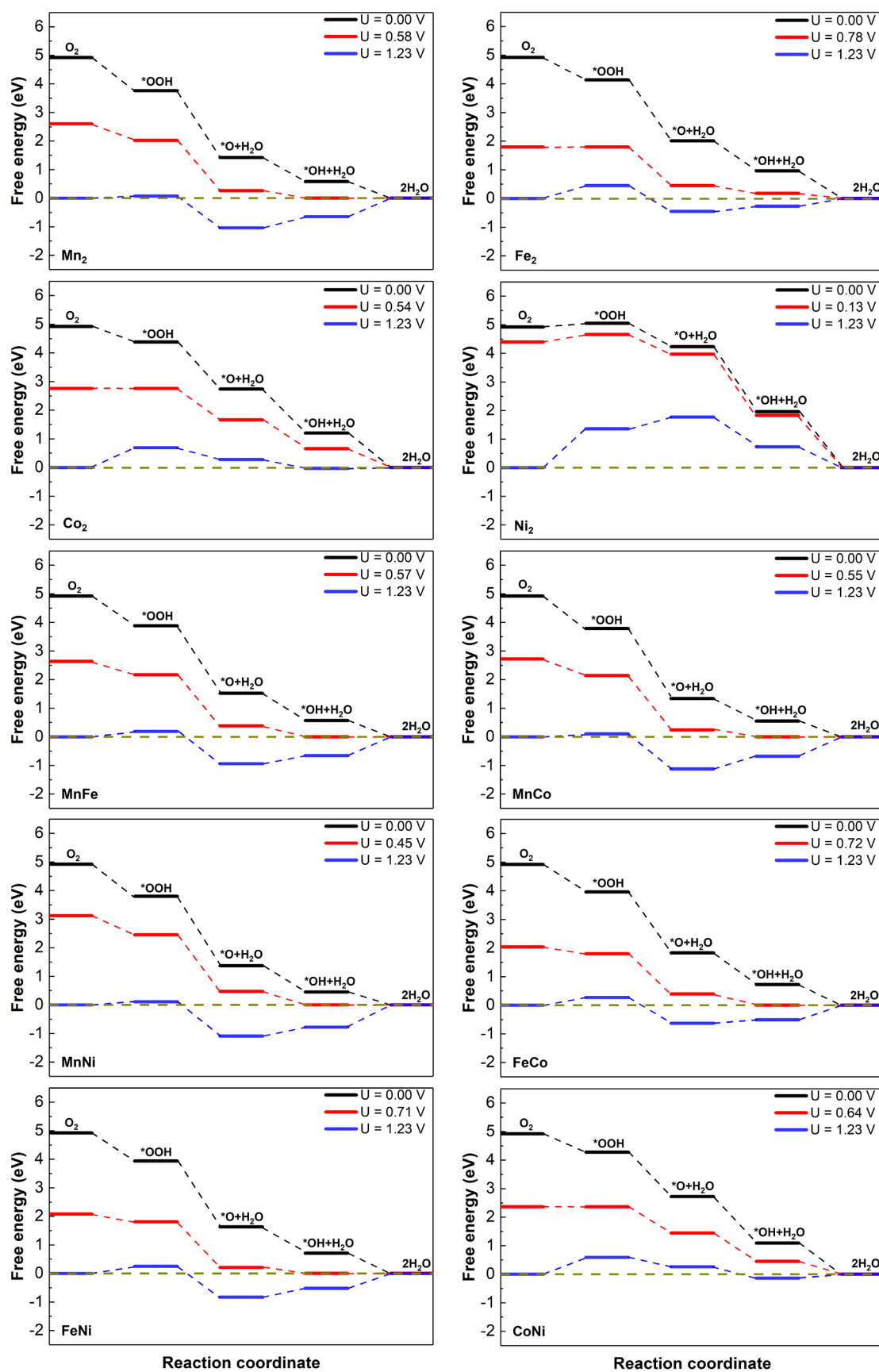


Fig. S12. The free energy diagrams of ORR for all UHD-DACs at different potentials for pathway-A.

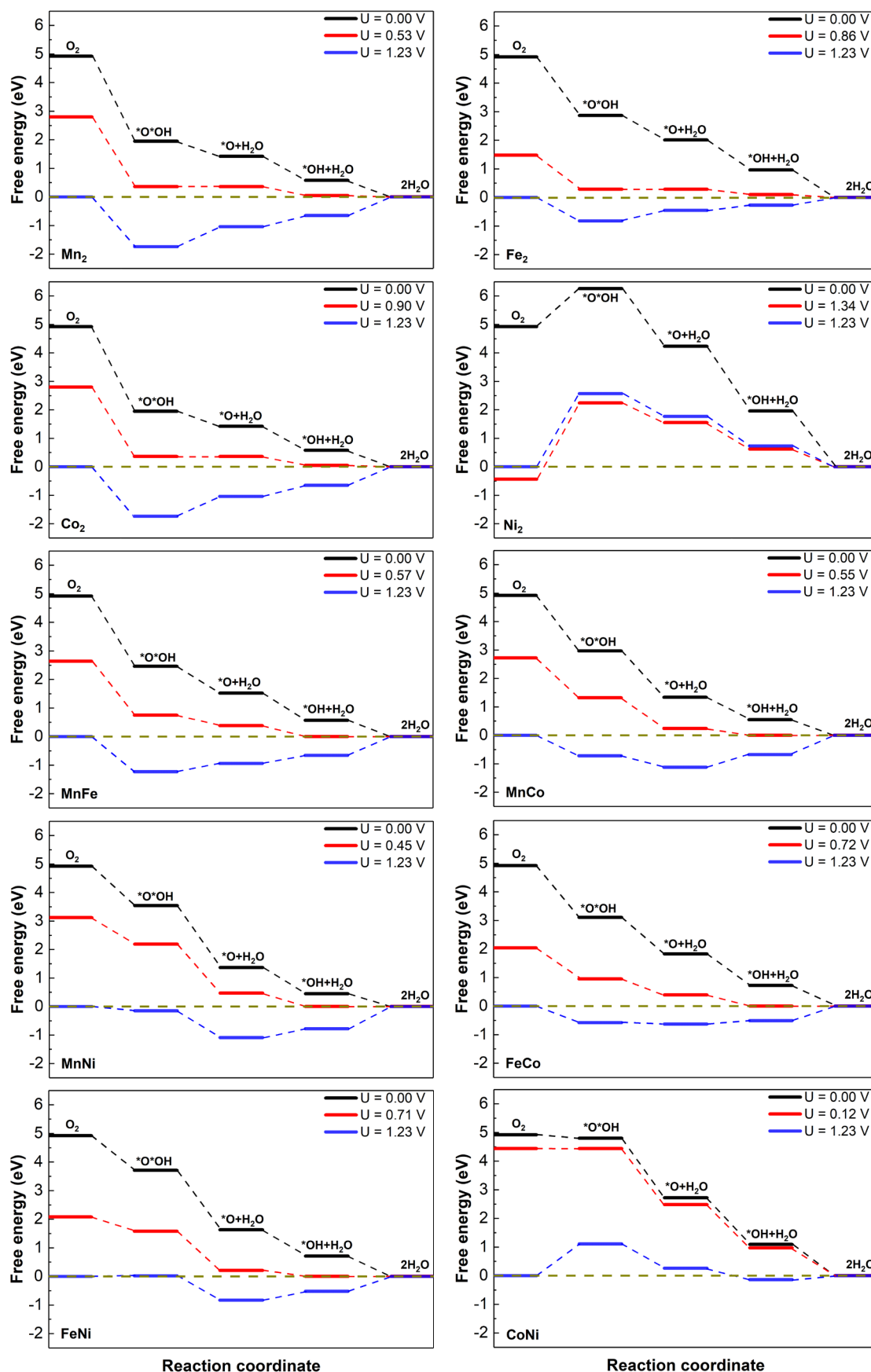


Fig. S13. The free energy diagrams of ORR for all UHD-DACs at different potentials for pathway-B.

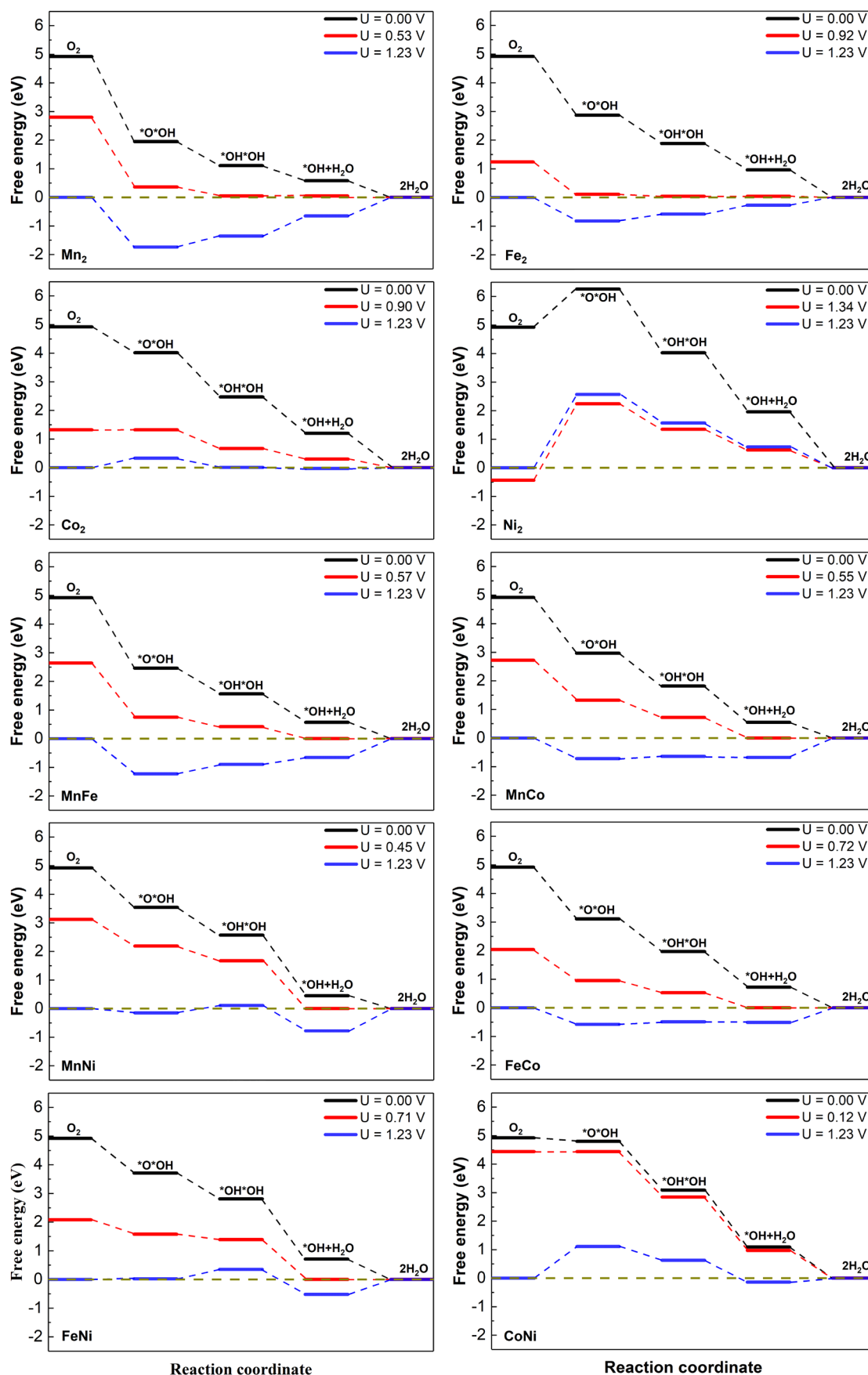


Fig. S14. The free energy diagrams of ORR for all UHD-DACs at different potentials for pathway-C.

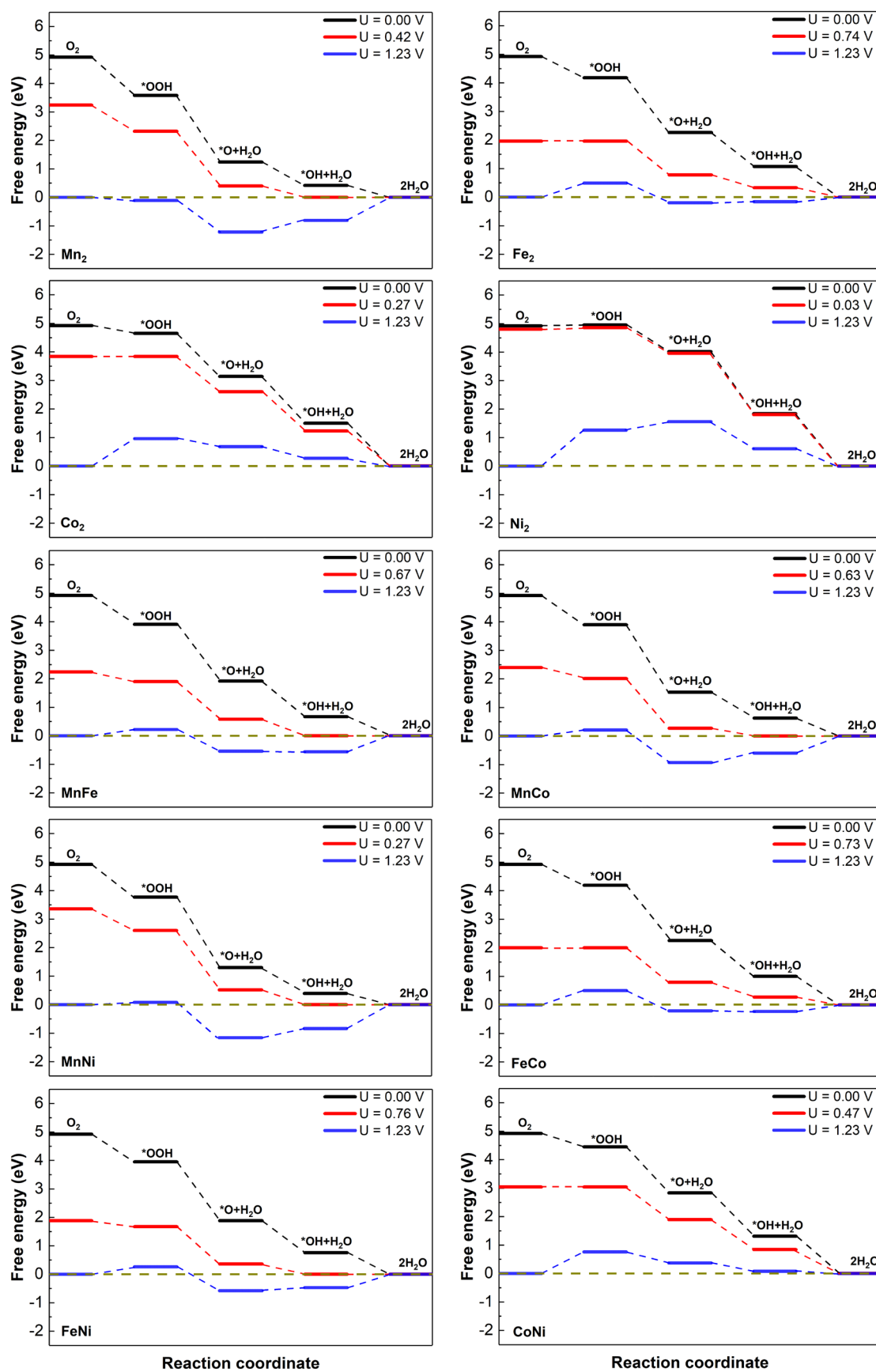


Fig. S15. The free energy diagrams of ORR for all LD-DACs at different potentials for pathway-A.

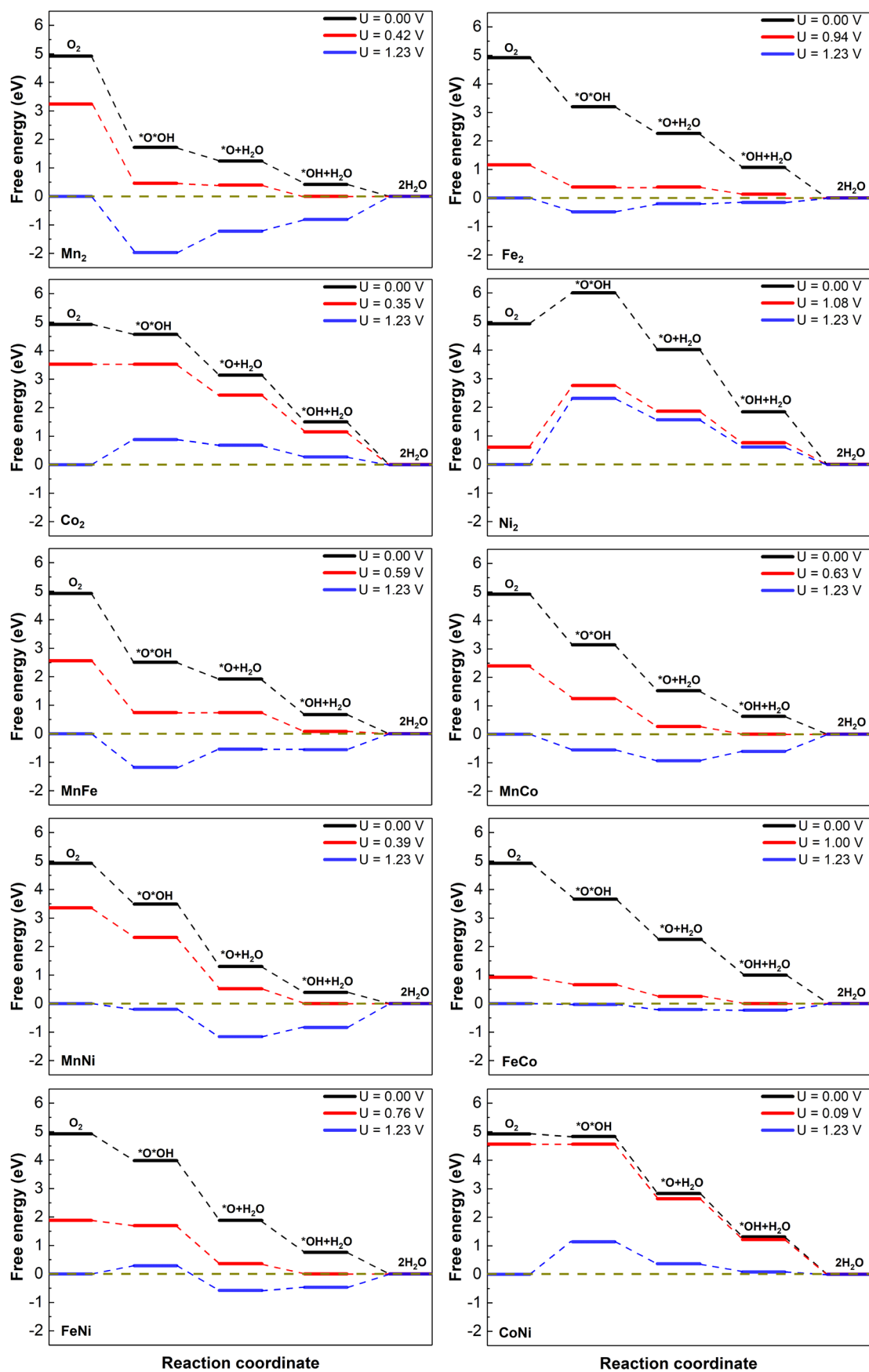


Fig. S16. The free energy diagrams of ORR for all LD-DACs at different potentials for pathway-B.

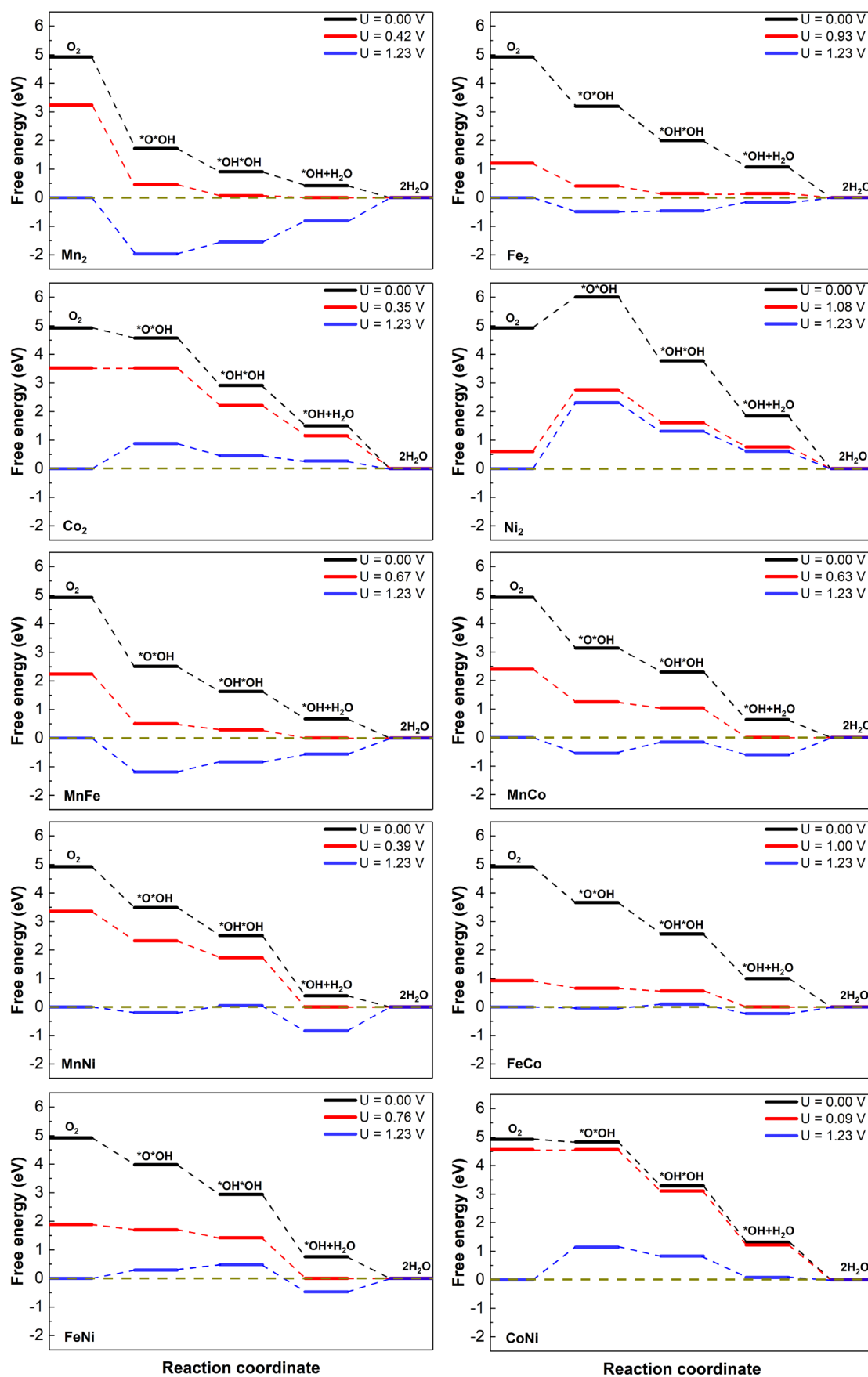


Fig. S17. The free energy diagrams of ORR for all LD-DACs at different potentials for pathway-C.

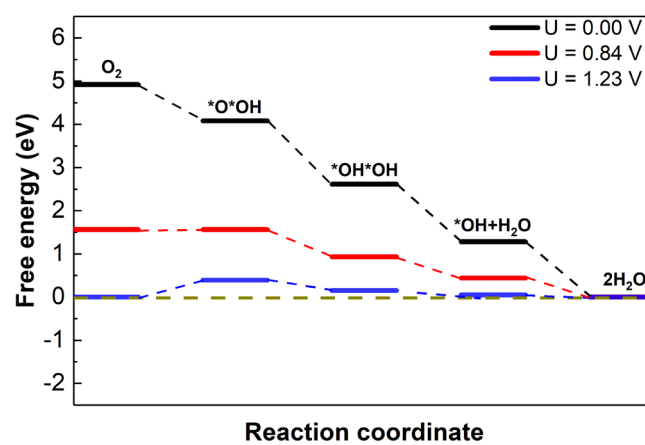


Fig. S18. The free energy diagrams of ORR for Co₂N₆ UHD-DAC at different potentials for pathway-C based on HSE06 functional.

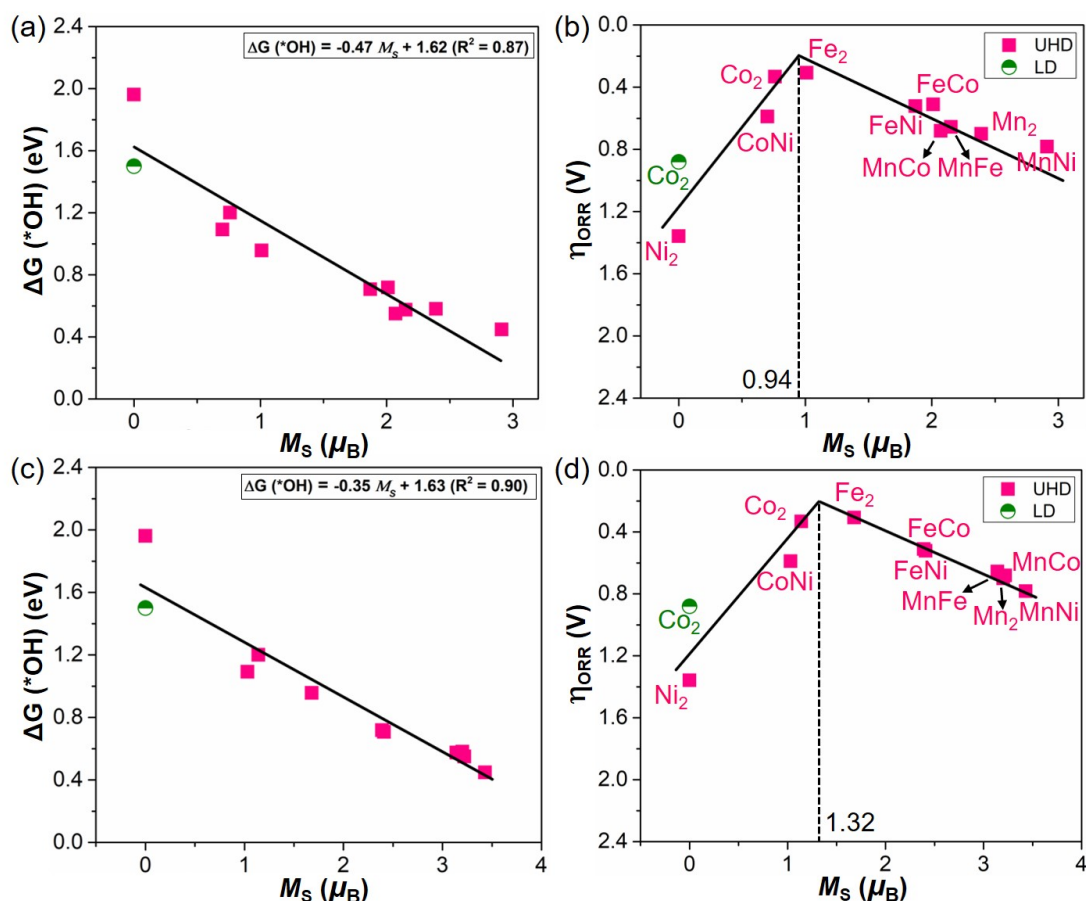


Fig. S19. (a)/(c) The scaling relationship between $\Delta G(*OH)$ for optimal pathway and the local spin magnetic moments (M_s) for the metal atom that anchor the $*OH$. (b)/(d) The volcano plots for the η_{ORR} for optimal pathway as the function of M_s . The pink and green marks represent the UHD- and LD-DACs, respectively. The upper (a-b) and bottom (c-d) results are calculated based on PBE and HSE06 functional, respectively. In the volcano plots (b) and (d), the critical spin magnetic moment corresponding to the optimal active point is also given from PBE and HSE06 functional, respectively.

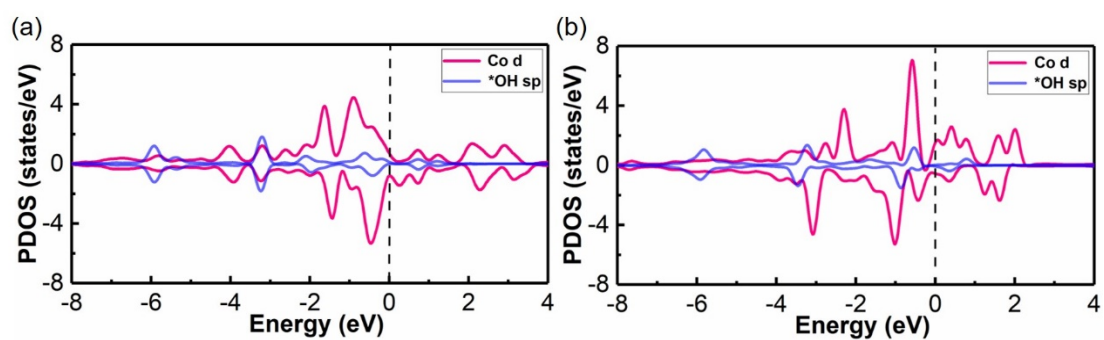


Fig. S20. The PDOS with electronic orbital interaction for Co_2N_6 (a) UHD- and (b) LD-DACs with $^*\text{OH}$ adsorption, including the Co $3d$ orbitals (pink) and $^*\text{OH}$ sp orbitals (blue) for DAC with OH^- adsorption, respectively. Here the Fermi level was set to 0.

Note S1. Solvation effect

Herein, the water configurations and solvation effects of the intermediates were obtained by molecular dynamics simulations (combining force-field molecular dynamic simulation implemented in LAMMPS [69] and *ab initio* molecular dynamic simulation in VASPsol [67]). The details are present below:

Firstly, we constructed a random explicit water model with a density of about 1 g/cm³, including 20 H₂O molecules. For this explicit solvent model with 20 H₂O molecules, we used the LAMMPS to conduct TIP3P [70] force-field molecular dynamic (MD) simulations for 5 ns with the NVT ensemble at 300 K. Then we added this explicit water model by LAMMPS to the catalyst surface to implement the *ab initio* MD simulations (AIMD) by VASPsol for 3 ps at 300 K. The final structures are used to obtain the explicit solvation energies of reaction species. The explicit structure model with 20 explicit water molecules for various adsorbed species on Mn₂N₆ UHD-DAC are shown in **Fig. S21** and the explicit solvation energies for different adsorbed species are shown in the **Table S6**. It is found that the solvation energies from the continuum solvation model by VASPsol are comparable with those from our explicit model and those of previous work with explicit model. [71] Moreover, the explicit solvation effect doesn't alter their optimal reaction pathway for ORR on both UHD- and LD-DACs (**Table S7**). Importantly, the solvation effect has a small influence on the η_{ORR} values, for which Fe₂N₆ and Co₂N₆ UHD-DACs still have the smallest η_{ORR} and deliver the highest ORR activity among all the UHD-DACs. These results indicate the reasonability of our computational methods for the ORR activity.

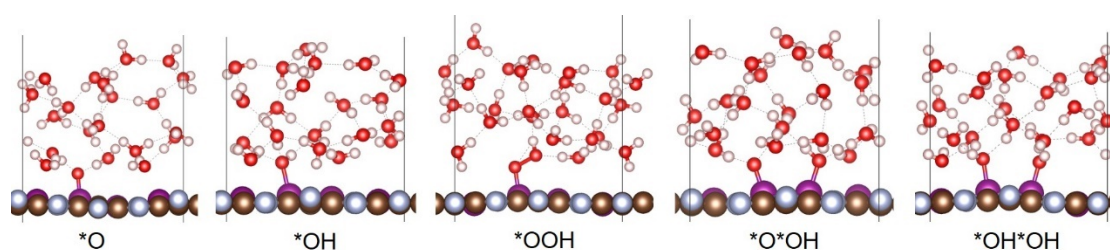


Fig. S21. The explicit structure model with 20 explicit water molecules for various adsorbed species on Mn₂N₆ UHD-DAC. Due to the large computational cost, here we only take Mn₂N₆ UHD-DAC as representative.

Table S6. The solvation energies (ΔE_{sol} , eV) for different adsorbed species. The explicit structure model with 20 explicit water molecules for various adsorbed species are shown in **Fig. S21**.

Species	ΔE_{sol} (implicit)	ΔE_{sol} (explicit)	ΔE_{sol} from Ref [18]	ΔE_{sol} from Ref [68]	ΔE_{sol} from Ref [59]	ΔE_{sol} from Ref [70]
*O	-0.29	-0.27	/	-0.29	/	0.36
*OH	-0.22	-0.30	-0.19	-0.38	-0.30	0.27
*OOH	-0.26	-0.37	/	-0.30	-0.30	0.21
*O*OH	-0.33	-0.33	-0.34	/	/	/
*OH*OH	-0.31	-0.52	-0.40	/	/	/

Table S7. The overpotentials of ORR (η_{ORR}) with implicit and explicit solvation effect through the optimal reaction pathway (A, B or C) over corresponding UHD- and LD-DACs.

DACs	η_{ORR} with implicit solvation effect		η_{ORR} with explicit solvation effect	
	UHD	LD	UHD	LD
Mn ₂	0.70 (C)	0.81 (C)	0.83 (C)	0.89 (C)
Fe ₂	0.31 (C)	0.29 (C)	0.44 (C)	0.32 (C)
Co ₂	0.33 (C)	0.88 (C)	0.33 (C)	0.88 (C)
Ni ₂	1.36 (A)	1.26 (A)	1.25 (A)	1.15 (A)
MnFe	0.66 (B)	0.56 (C)	0.74 (B)	0.64 (C)
MnCo	0.68 (B)	0.60 (B)	0.76 (B)	0.67 (B)
MnNi	0.78 (B)	0.84 (B)	0.86 (B)	0.91 (B)
FeCo	0.51 (B)	0.23 (B)	0.59 (B)	0.31 (B)
FeNi	0.52 (B)	0.47 (B)	0.60 (B)	0.55 (B)
CoNi	0.59 (A)	0.76 (A)	0.48 (A)	0.65 (A)

References

- [18] W. Zou, R. Lu, X. Liu, G. Xiao, X. Liao, Z. Wang, and Y. Zhao, *Theoretical Insights into Dual-Atom Catalysts for the Oxygen Reduction Reaction: The Crucial Role of Orbital Polarization*, J. Mater. Chem. A **10**, 9150 (2022).
- [58] J. Greeley and J. K. Nørskov, *Electrochemical Dissolution of Surface Alloys in Acids: Thermodynamic Trends from First-Principles Calculations*, Electrochim. Acta **52**, 5829 (2007).
- [59] X. Guo, S. Lin, J. Gu, S. Zhang, Z. Chen, and S. Huang, *Simultaneously Achieving High Activity and Selectivity toward Two-Electron O₂ Electroreduction: The Power of Single-Atom Catalysts*, ACS Catal. **9**, 11042 (2019).

- [67]K. Mathew, R. Sundararaman, K. Letchworth-Weaver, T. A. Arias, and R. G. Hennig, *Implicit Solvation Model for Density-Functional Study of Nanocrystal Surfaces and Reaction Pathways*, J. Chem. Phys. **140**, 084106 (2014).
- [68]G. Xiao, R. Lu, J. Liu, X. Liao, Z. Wang, and Y. Zhao, *Coordination Environments Tune the Activity of Oxygen Catalysis on Single Atom Catalysts: A Computational Study*, Nano Res. **15**, 3073 (2022).
- [69]S. Plimpton, *Fast Parallel Algorithms for Short-Range Molecular Dynamics*, J Comput. Phys. **117**, 1 (1995).
- [70]W. L. Jorgensen, J. Chandrasekhar, J. D. Madura, R. W. Impey, and M. L. Klein, *Comparison of Simple Potential Functions for Simulating Liquid Water*, J. Chem. Phys. **79**, 926 (1983).
- [71]M. Reda, H. A. Hansen, and T. Vegge, *DFT Study of Stabilization Effects on N-Doped Graphene for ORR Catalysis*, Catal Today **312**, 118 (2018).